



**HAL**  
open science

# Robust Nonlinear Control of a Power Flow Controller for Meshed DC Grids

Tanguy Simon, Jean-François Trégouët, Xuefang Lin-Shi, Hervé Morel

► **To cite this version:**

Tanguy Simon, Jean-François Trégouët, Xuefang Lin-Shi, Hervé Morel. Robust Nonlinear Control of a Power Flow Controller for Meshed DC Grids. *Control Engineering Practice*, 2022, 131, 10.1016/j.conengprac.2022.105389 . hal-03860875

**HAL Id: hal-03860875**

**<https://hal.science/hal-03860875>**

Submitted on 18 Nov 2022

**HAL** is a multi-disciplinary open access archive for the deposit and dissemination of scientific research documents, whether they are published or not. The documents may come from teaching and research institutions in France or abroad, or from public or private research centers.

L'archive ouverte pluridisciplinaire **HAL**, est destinée au dépôt et à la diffusion de documents scientifiques de niveau recherche, publiés ou non, émanant des établissements d'enseignement et de recherche français ou étrangers, des laboratoires publics ou privés.

## Highlights

### **Robust Nonlinear Control of a Power Flow Controller for Meshed DC Grids**

Tanguy Simon, Jean-François Trégouët, Xuefang Lin-Shi, Hervé Morel

- Robustness to high parametric variations is necessary for power flow controllers.
- This new control law is robust to any relevant grid parameters
- The tuning of the control law is simple and intuitive.
- Formal proofs of stability are given based on Singular Perturbations theory.
- Experimental results validate the approach.

# Robust Nonlinear Control of a Power Flow Controller for Meshed DC Grids

Tanguy Simon<sup>a</sup>, Jean-François Trégouët<sup>a,\*</sup>, Xuefang Lin-Shi<sup>a</sup>, Hervé Morel<sup>a</sup>

<sup>a</sup>*Univ Lyon, INSA Lyon, Université Claude Bernard Lyon 1, Ecole Centrale de Lyon, CNRS, Ampère, UMR5005, 69621, Villeurbanne, France*

---

## Abstract

The studied power flow controller is an electronic device capable of controlling the power flows at a node in a meshed low voltage DC grid. It is made of  $m$  buck-boost converters connected in parallel on their high voltage-side to a reservoir capacitor. This paper proposes a nonlinear control method achieving robust regulation of the power in each line and of the reservoir voltage inside the converter. This control law only requires measurements of local currents and voltages, and the knowledge of the maximum possible resistance of the grid, whereas prior control laws required the full knowledge of some nominal parameters. Proofs of stability are given for every possible uncertain parameters of the studied grid model whereas prior control laws were only valid at nominal parameters and their neighbourhood. The performance of this control method is asserted through a tenth-scale experimental set-up. Stochastic simulations are conducted to estimate the basin of attraction.

*Keywords:* Power flow controller, Microgrid, Meshed DC grid, Singular perturbations, Robust control

---

## 1. Introduction

Microgrids are small-scale electric networks made of distributed generation units, loads and a control system, and are either connected to a main utility grid or islanded from it. By their local scale and their flexibility, microgrids are a key enabler of Renewable/Citizen Energy Communities (R/CECs), detailed in (Caramizaru and Uihlein, 2020). Generally designed to ease the integration of distributed renewable energy generators, microgrids can play an important role in the transition to a greener grid, as some of the intermittency can be coped with locally (adaptation of the demand to the local production, local storage). See (Hatziargyriou, 2014) for more details on microgrids.

The use of DC instead of AC brings various advantages such as removing the problem of reactive power and limiting the number of power converters when many DC loads and generation units are used (Anand and Fernandes, 2010). In particular, it has been shown that – depending on the utilization, structure, and layout of the buildings and the efficiency of the main Voltage Source Converter – the transition to DC could improve the environmental impact of microgrids (Kockel et al., 2022).

The meshed structure in microgrids improves its resiliency, flexibility and is the natural structure when loads and renewable generators are randomly distributed, see

(Mackay et al., 2015), (Simon et al., 2021b) and the recent surveys (Fotopoulou et al., 2021; Mackay et al., 2017; Prakash et al., 2016).

The Power Flow Controllers (PFC)<sup>1</sup> are also called Current Flow Controllers (Balasubramaniam et al., 2019), Dynamic Energy Routers (Ramirez et al., 2014) or Smart Nodes (Zafeiratou et al., 2018). They are necessary power electronic devices in the context of meshed grids to manage the distribution of the power between the multiple paths and prevent the overloading of some lines. They can also be useful to manage power exchanges between microgrids (Vuyyuru et al., 2019). This can be done with series-connected converters, which insert a small voltage in series with the line (Balasubramaniam et al., 2019; Purgat et al., 2017) or with shunt-connected converters which modify the power flow by controlling the line voltage, and which are mainly designed for low voltage grids (Jovcic and Ooi, 2010; Natori et al., 2018). Although series-connected PFCs are generally more efficient than shunt-connected ones (Natori et al., 2017), the latter are capable of filling in other essential functions such as DC circuit breaking and line voltage regulation. They are therefore a more versatile module for the control of renewable-based microgrids.

This paper is focused on the control of a multi-terminal shunt-connected DC PFC placed at a node of the grid, as drawn in Fig. 1. The architecture of the converter is presented in Fig. 2. The work presented in this paper lies at the lowest (primary) control level: It is assumed that

---

\*Corresponding author. Phone: +33 6 16 48 58 30. PhD work financed through a public contract by INSA Lyon, France.

*Email addresses:* [tanguy.simon@insa-lyon.fr](mailto:tanguy.simon@insa-lyon.fr) (Tanguy Simon), [jean-francois.tregouet@insa-lyon.fr](mailto:jean-francois.tregouet@insa-lyon.fr) (Jean-François Trégouët), [xuefang.shi@insa-lyon.fr](mailto:xuefang.shi@insa-lyon.fr) (Xuefang Lin-Shi), [herve.morel@insa-lyon.fr](mailto:herve.morel@insa-lyon.fr) (Hervé Morel)

---

<sup>1</sup>Note that Power Flow Controller refers to a physical device and not a control law.

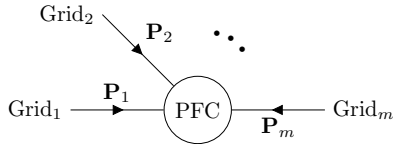


Figure 1: The PFC at an  $m$ -terminal node in the grid

the power references to be tracked are given by a higher (secondary) level controller such as the ones discussed in (Nasirian et al., 2015; Casavola et al., 2017; Cucuzzella et al., 2019). For these papers and power flow studies such as (Benedito et al., 2019; Jeeninga et al., 2020), the PFC can be seen as a controllable power router, adding a degree of freedom in distributed or centralised control schemes.

The control of shunt-connected DC PFCs has been addressed in a few papers. Among them, recall a multi-terminal PFC (Takahashi et al., 2015) improved in (Natori et al., 2018), a similar three-branch PFC in (Ramirez et al., 2014) and a PFC made of two separate Split-PI converters (Barara et al., 2017). The main shortcomings of (Takahashi et al., 2015; Natori et al., 2018; Barara et al., 2017) are the absence of dynamic model, proof of stability and proof of robustness. No direct control of the power is achieved, and the control laws are applied to two-terminal devices, which do not constitute a node. Each converter connected to a grid should be able to function with minimal non-local information to reduce the need for heavy communication infrastructures and the vulnerability to loss of information and cyber-attacks. In (Takahashi et al., 2015), the control law is a constant ratio determined by a look-up table, based on the knowledge of the voltage at the end of the line, an uncertain parameter in practice. In (Natori et al., 2018), a PI controller is used to regulate the current instead of the power, whose reference is again computed using the voltage at the end of the line. Moreover, the reservoir voltage, which is the voltage on a capacitor inside the converter, is not controlled and can drift outside the physical boundaries. The experiments are conducted by imposing this voltage using an auxiliary power supply. In (Ramirez et al., 2014), different control strategies are proposed: a PI controller and an approximated feedback linearisation controller. These strategies are based on current control, with a current reference computed by dividing the power reference by the line voltage. This voltage is a state of the system and evolves on the same timescale as the current. As detailed further in Sec. 4, this implies that the method used to compute the gains does not ensure the stability of the equilibrium. Moreover, no asymptotic convergence to the objectives is observed with both controllers. Eventually, in (Barara et al., 2017), the authors propose a current-limited voltage controller using the RST technique with hysteresis switching. The reservoir voltage is properly controlled but direct power flow control is not achieved.

This article continues a series of studies on the regulation of an  $m$ -terminal low voltage DC PFC drawn in Fig.2

(Simon et al., 2021b; Lin-Shi et al., 2021; Simon et al., 2021a). As explained in (Simon et al., 2021b), the system formed by the PFC and the microgrid can be modelled using a bilinear state-space model with uncertain parameters and a second-order polynomial output. While many papers dealing with stabilisation problems for bilinear systems can be found in the literature (see for instance, (Gutman, 1981; Longchamp, 1980; Tarbouriech et al., 2009)), very few addressed the more general problem of output regulation, e.g., (Grasselli et al., 1979), and more recently (Cisneros et al., 2015; Tang et al., 2006). Moreover, all of them focus on systems having a pure linear output and are therefore not directly applicable to the problem explained above. After the addition of integrators on the output error for steady-state accuracy, the augmented system becomes polynomial with uncertain coefficients. Since the aim is to prove the stability of such a system on a large parametric set, no systematic method exists.

The Forwarding method (Astolfi and Praly, 2017; Zitte et al., 2020), can be applied to nonlinear systems with nonlinear outputs with some local robustness properties. It has been applied to the PFC problem in (Simon et al., 2021a), yielding interesting results. The main concern of our paper is to improve the theoretical results of (Simon et al., 2021a) through a new control method designed specifically for the PFC problem. First, in (Simon et al., 2021b,a), the proofs of stability are given for a nominal vector of parameters and nominal references. Although it is proven in (Simon et al., 2021a) that sufficiently small disturbances of those parameters or references would not destabilise the system, it is unclear whether or not these control laws would be suitable for the high uncertainty of a microgrid. In (Lin-Shi et al., 2021), the uncertainty of the grid is not taken into account directly, and strong hypotheses are taken to simplify the design. Second, the previous control laws rely on the measurement of at least the current and the voltage in each line in addition to a reservoir voltage inside the controller. Third, the tuning of those laws is not straightforward since it involves pole placement or the choice of gain matrices. Eventually, since these control laws are only valid for a nominal set-point and its neighbourhood, a question is left in the design: Which is the best "nominal set-point" around which the control law can be designed to achieve the best robustness?

In regard to these limitations, the proposed method achieves the following contributions: 1) Proofs of stability are given for all possible parameters and references describing the microgrid. 2) The necessary measurements are reduced to the current in each line in addition to the reservoir voltage inside the converter instead of a full state feedback. This improves the implementability of the control law and means that a simple 3-phase inverter can be re-purposed to create a 3-terminal PFC by adding an  $LC$  filter on each phase. 3) Only three gains need to be tuned, and their tuning is intuitive. 4) The control law only requires the knowledge of the maximum resistance in the grid for its tuning, and is valid for every possible set-point. There is

Table 1: Nomenclature

Electrical			
$C_R$	Reserv. cap.	$\mathbf{v}_R$	Reserv. volt. (on $C_R$ )
$L$	Filter induct.	$\mathbf{i}_k, i_k$	Filter current (in $L$ )
$C$	Filter cap.	$\mathbf{v}_k, v_k$	Line voltage (on $C$ )
$L_{Gk}$	Grid induct.	$\mathbf{i}_{Gk}, i_{Gk}$	Grid current
$R_{Gk}$	Grid resist.	$V_{Gk}$	Grid voltage
$\mathbf{P}_k$	Power in line $k$	$\mathbf{d}$	Duty cycle vector
State-space			
$\mathbf{z}_k$	Power Integrator	$\theta$	Parameter vector
$\zeta, \zeta$	Voltage integrator	$r$	Reference vector
$x$	Slow state vector	$(\theta, r)$	Set-point vector
$\eta$	Fast state vector	$\psi_k$	Slow state
Sets			
$\Theta$	Possible param.	$\mathcal{E}(\theta, r)$	Controlled equi. points
$\mathcal{R}$	Possible ref.	$\mathcal{S}$	Admiss. set-points
Indexes and exponents			
<b>bold</b>	Absolute coord.	$r$	Reference
<i>slim</i>	Error coord.	$*$	Equilibrium

no need to choose which "nominal set-point" would be the best.

The paper is organised as follows: In Sec. 2, the converter topology is presented, its dynamic model is given along with the conditions for the existence of solutions. In Sec. 3, the proposed control law is given in the main theorem, and its proof follows. In Sec. 4, the proposed control law is compared to the relevant published literature. The experimental results are presented in Sec. 5 along with stochastic simulations, and the conclusion is written in Sec. 6. The technical proofs of lemmas and propositions are postponed to the appendix.

**Notation.** The operator "diag  $\{\}$ " builds a diagonal matrix from entries of the input vector argument. "Im( $\cdot$ )" builds the linear space spanned by its input vectors. Given a vector  $a \in \mathbb{R}^n$ , the notation  $a_k$  refers to the  $k$ -th element of  $a$ , with 1 being the index of the first element. The null matrix of size  $m \times n$  is denoted by  $\mathbf{0}_{m \times n}$  while  $\mathbf{0}_m$  denotes column vectors. Dimensions are omitted when obvious from the context. Note  $\llbracket 1, m \rrbracket$  as every integer between 1 and  $m$  included, i.e.  $\llbracket 1, m \rrbracket = \{1, \dots, m\}$ . Given a set  $\mathcal{S}$ ,  $\text{card}(\mathcal{S})$  denotes its cardinality. A summary of the notation used is shown in Table 1 to aid the reader.

## 2. Problem Statement and Modelling

### 2.1. Converter topology

The chosen topology for the PFC to function as a smart-node as shown in Fig. 1 is given in Fig. 2, where the integer  $m$  refers to the number of branches. This number should be greater than one for it to properly operate (at least one power input and one power output), and greater than two to have a node. The device is made of  $m$  buck-boost converters connected in parallel on their high-side

to a reservoir capacitor  $C_R$ , which acts as a small energy buffer between the branches. Each line is connected to the positive and negative terminals of a branch ( $+(k)$  and  $-(k)$ ).

Note the following fact.

**Fact 1.** The reservoir voltage is always strictly positive:  $\mathbf{v}_R(t) > 0 \forall t \geq 0$ .  $\triangle$

Indeed, in any relevant operating conditions, as long as the microgrid is turned on, at least one of the line voltages  $\mathbf{v}_k$  is strictly positive. If  $\mathbf{v}_R < \max_k(\mathbf{v}_k)$ , the anti-parallel diode of the corresponding upper IGBT opens, and a current flows through it, charging  $C_R$  until  $\mathbf{v}_R \approx \max_k(\mathbf{v}_k)$ . This is a rapid phenomenon independent of the control law driving the IGBTs.

### 2.2. Specifications and Control Objectives

The PFC modifies the power flow in the grid by slightly changing the line voltage at each terminal. The grid context adds a strong constraint: These line voltages should be maintained within a tolerance of  $\pm \Delta \mathbf{v}$  around the nominal voltage  $\mathbf{v}^n > 0$ . In this paper, only steady-state voltage constraints are considered, i.e.  $\mathbf{v}(t)$  might escape from  $\mathbf{v}^n \pm \Delta \mathbf{v}$  during transient but must asymptotically reach a constant value within this interval.

**Assumption 1.** The steady-state maximum required voltage deviation satisfies  $\Delta \mathbf{v} < \frac{1}{3} \mathbf{v}^n \Leftrightarrow \frac{\Delta \mathbf{v}}{\mathbf{v}^n} < \frac{1}{3}$ .  $\triangle$

Typically, the required tolerance does not exceed  $\Delta \mathbf{v} / \mathbf{v}^n = 10\%$ , so that the previous assumption is verified in any relevant practical situation (IEEE-SA, 2009). In other words, the required assumption is less demanding than the tolerances required by the power grid application.

The objective of the PFC is to control the electric power flowing through each of its terminals. For any stationary steady-state, the voltage  $\mathbf{v}_R$  is kept constant. Therefore, its energy is also constant, which implies that the sum of steady-state powers  $\mathbf{P}_k$  is zero. As a consequence, if  $\mathbf{P}_1, \dots, \mathbf{P}_{m-1}$  and  $\mathbf{v}_R$  are maintained at a constant reference, then the last power  $\mathbf{P}_m$  will naturally converge to the overall power balance and is therefore not included in the control objectives.

In Fig. 3 the  $k$ -th branch of the PFC is drawn on the left, while the right side of the dashed line is an equivalent circuit model of the rest of the grid as seen by this branch. In this paper, PWM switching of each branch is assumed, and the converter is controlled through the duty cycles (ratios)  $\mathbf{d}_k$ , which take values in  $[0, 1]$ . Note that the average voltage at the middle point of the half-bridge is  $\mathbf{v}_R \mathbf{d}_k$ . It follows that for a given middle point voltage, the lower  $\mathbf{v}_R$  is, the higher the duty cycles will be, with a risk of saturation of  $\mathbf{d}_k$  at the upper bound. The reservoir voltage should therefore be maintained at a sufficiently high reference. The references to be tracked are therefore contained in the set  $\mathcal{R} \subseteq \mathbb{R}^m$ , defined as follows:

$$\mathcal{R} := \left\{ r = (\mathbf{P}_1^r, \dots, \mathbf{P}_{m-1}^r, \mathbf{v}_R^r) \in \mathbb{R}^m : \mathbf{v}_R^r > \mathbf{v}^n + \Delta \mathbf{v} \right\}. \quad (1)$$

These references are considered given by a higher level algorithm, and their tracking should be achieved despite the high variability of the grid.

### 2.3. Modelling

In Fig. 3, the grid parameters ( $L_{Gk}$ ,  $R_{Gk}$  and  $V_{Gk}$ ) for each line are considered unknown from the PFC's viewpoint. The dynamical model for **Grid** <sub>$k$</sub>  in Fig. 3 will therefore be uncertain. The filter current vector is denoted by  $\mathbf{i}$ , the line voltage vector by  $\mathbf{v}$  and the grid current vector by  $\mathbf{i}_G$ . Refer to Tab. 1 for the nomenclature. The dynamic model of the system can be found using the electrical laws for the current and voltage in inductors and capacitors, respectively, while assuming ideal components and switches (see (Simon et al., 2021b)). The signals are averaged over a switching period and the input vector  $\mathbf{d} = [\mathbf{d}_1, \dots, \mathbf{d}_m]^\top \in \mathbb{R}^m$  is made of the duty ratios. The state-space model then writes:

$$\frac{d}{dt} \mathbf{v}_R = \frac{1}{C_R} \sum_{k=1}^m \mathbf{i}_k \mathbf{d}_k, \quad (2a)$$

$$\frac{d}{dt} \mathbf{i}_k = \frac{1}{L} (\mathbf{v}_k - \mathbf{v}_R \mathbf{d}_k), \quad (2b)$$

$$\frac{d}{dt} \mathbf{v}_k = \frac{1}{C} (\mathbf{i}_{Gk} - \mathbf{i}_k), \quad (2c)$$

$$\frac{d}{dt} \mathbf{i}_{Gk} = \frac{1}{L_{Gk}} (V_{Gk} - \mathbf{v}_k - R_{Gk} \mathbf{i}_{Gk}), \quad (2d)$$

$$\mathbf{P}_k = \mathbf{i}_k \mathbf{v}_R \mathbf{d}_k, \quad (2e)$$

for  $k \in \llbracket 1, m \rrbracket$ .

The uncertain model parameters are gathered in the vector  $\theta \in \mathbb{R}^{3m}$ . Let  $\Theta \subset \mathbb{R}^{3m}$  be the non-empty set of possible parameters that are compatible with the physics of the system and the constraints of the application. It is defined as

$$\Theta := \left\{ \theta \in \mathbb{R}^{3m} : L_{Gk} > 0, \underline{R} \leq R_{Gk} \leq \bar{R}, \right. \\ \left. 0 \leq V_{Gk} \leq \mathbf{v}^n + \Delta \mathbf{v}, (k \in \llbracket 1, m \rrbracket) \right\}. \quad (3)$$

These constraints are justified as follows:  $L_{Gk}$ ,  $R_{Gk}$  represent physical properties (inductance and resistance) which are always strictly positive, hence  $\underline{R} > 0$ . The bounds on  $R_{Gk}$  must be chosen to appropriately represent possible loads and lines on the grid (See Sec. 5 for numerical values). It is considered that, should the PFC be turned off, the line voltage does not naturally become negative or surpass its maximum  $\mathbf{v}^n + \Delta \mathbf{v}$ , hence the bounds on  $V_{Gk}$ . Values below  $\mathbf{v}^n - \Delta \mathbf{v}$  are considered to allow for grid models behaving in steady-state as pure resistive loads.

### 2.4. Problem formulation

Before defining the precise control problem tackled in this paper, it is necessary to define the conditions under which it will be feasible.

As stated before, the line voltage  $\mathbf{v}_k$  should be contained in  $]\mathbf{v}^n - \Delta \mathbf{v}, \mathbf{v}^n + \Delta \mathbf{v}[$ . In regard to these constraints, not

all the equilibrium points  $(\mathbf{v}_R^*, \mathbf{i}^*, \mathbf{v}^*, \mathbf{i}_G^*, \mathbf{d}^*) \in \mathbb{R}^{4m+1}$  will be acceptable.

Define the set  $\mathcal{E}(\theta, r)$  as the set of appropriate controlled equilibrium points.

$$\mathcal{E}(\theta, r) := \left\{ (\mathbf{v}_R^*, \mathbf{i}^*, \mathbf{v}^*, \mathbf{i}_G^*, \mathbf{d}^*) : (2a) \text{ to } (2d) = 0, \right. \\ \left. \mathbf{v}^n - \Delta \mathbf{v} < \mathbf{v}_k^* < \mathbf{v}^n + \Delta \mathbf{v}, (k \in \llbracket 1, m \rrbracket) \right. \\ \left. \mathbf{P}_k^* = \mathbf{P}_k^r, (k \in \llbracket 1, m-1 \rrbracket), \mathbf{v}_R^* = \mathbf{v}_R^r \right\}. \quad (4)$$

The set  $\mathcal{S}$  gathers the parameters and references such that there exists a controlled equilibrium point, i.e.

$$\mathcal{S} := \left\{ (\theta, r) \in \Theta \times \mathcal{R} : \text{card}(\mathcal{E}(\theta, r)) > 0 \right\}. \quad (5)$$

As stated in the following lemma, this set can be defined more explicitly. Its proof can be found in Appendix A.

**Lemma 1.** *The set  $\mathcal{S}$  reads*

$$\mathcal{S} = \left\{ (\theta, r) \in \Theta \times \mathcal{R} : \Pi_k(\theta, r) > 0, \right. \\ \left. \mathbf{v}^n - \Delta \mathbf{v} < \frac{1}{2} \left( V_{Gk} + \sqrt{\Pi_k(\theta, r)} \right) < \mathbf{v}^n + \Delta \mathbf{v}, (k \in \llbracket 1, m \rrbracket) \right\},$$

with

$$\Pi_k(\theta, r) := V_{Gk}^2 - 4R_{Gk} \mathbf{P}_k^r, \quad (6)$$

$$\mathbf{P}_m^r := - \sum_{k=1}^{m-1} \mathbf{P}_k^r. \quad (7)$$

Furthermore, for any  $(\theta, r) \in \mathcal{S}$ ,  $\text{card}(\mathcal{E}(\theta, r)) = 1$ .

The set  $\mathcal{S}$  gathers all the set-points for which the stability should be proven.

**Remark.** It is assumed that the references in  $r$  are given by a higher level algorithm, such as the microgrid supervisor. These references are supposed to be appropriately computed, i.e. such that  $(\theta, r) \in \mathcal{S}$ .  $\lrcorner$

The control problem can now be formulated:

**Problem 1.** Find mappings  $\alpha$  and  $\beta$  such that for any parameters  $\theta$  and references  $r$  such that  $(\theta, r) \in \mathcal{S}$ , the resulting trajectories of system (2) in closed-loop with the regulator

$$\dot{\sigma} = \alpha(\sigma, \mathbf{v}_R, \mathbf{i}, \mathbf{v}, \mathbf{i}_G), \quad (8)$$

$$\mathbf{d} = \beta(\sigma, \mathbf{v}_R, \mathbf{i}, \mathbf{v}, \mathbf{i}_G) \quad (9)$$

are bounded forward in time and  $\lim_{t \rightarrow +\infty} \mathbf{y}(t) = r$ , with  $\mathbf{y} := (\mathbf{P}_1, \dots, \mathbf{P}_{m-1}, \mathbf{v}_R)$ .  $\bullet$

## 3. Main Results

The main result of this paper is given by the following theorem:

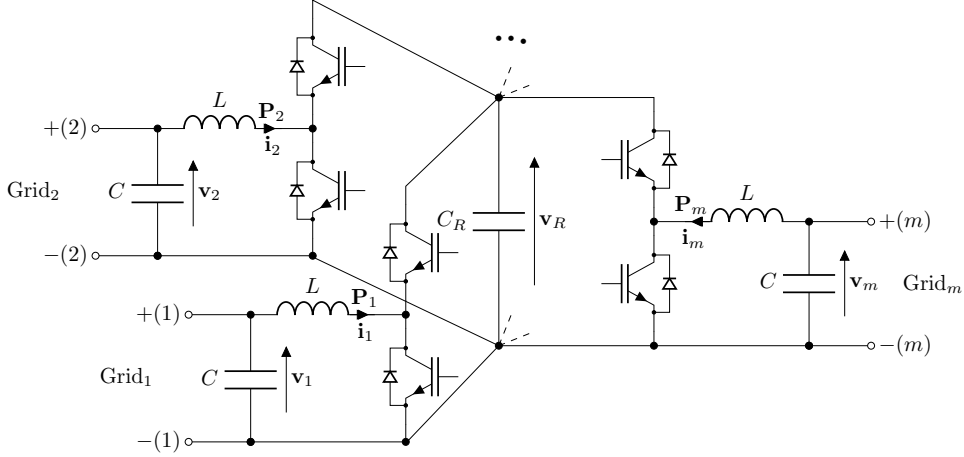


Figure 2: The chosen topology for the PFC, made of  $m$  buck-boost converters connected to a single reservoir capacitor  $C_R$ .

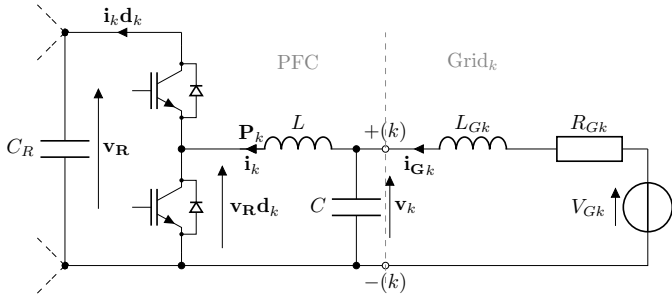


Figure 3: Detail of the  $k$ -th branch of the PFC (left) and the proposed grid model as seen by this terminal (right)

**Theorem 1.** For any  $k_{iv} > 0$ ,  $k_p \geq 0$ ,  $\delta$  such that  $0 < \delta < \mathbf{v}^n - 3\Delta\mathbf{v}$  and  $k_{iP} > mk_{iv}/l(\delta)$ , with

$$l(\delta) = \frac{\delta}{R + k_p}, \quad (10)$$

there exists  $\bar{\varepsilon} > 0$  such that for all  $0 < \varepsilon < \bar{\varepsilon}$ , the control law

$$\dot{\mathbf{z}}_k = \varepsilon k_{iP}(\mathbf{P}_k - \mathbf{P}_k^r), \quad (k \in \llbracket 1, m-1 \rrbracket), \quad (11a)$$

$$\dot{\boldsymbol{\zeta}} = \varepsilon k_{iv}(\boldsymbol{\nu}(\mathbf{v}_R) - \boldsymbol{\nu}(\mathbf{v}_R^r)), \quad (11b)$$

$$\mathbf{d}_k = \frac{1}{\mathbf{v}_R} (k_p \mathbf{i}_k + \mathbf{z}_k + \boldsymbol{\zeta}), \quad (k \in \llbracket 1, m-1 \rrbracket), \quad (11c)$$

$$\mathbf{d}_m = \frac{1}{\mathbf{v}_R} \left( k_p \mathbf{i}_m + \boldsymbol{\zeta} + \boldsymbol{\nu}(\mathbf{v}_R) - \boldsymbol{\nu}(\mathbf{v}_R^r) - \sum_{k=1}^{m-1} \mathbf{z}_k \right), \quad (11d)$$

where  $\boldsymbol{\nu} : \mathbb{R} \rightarrow \mathbb{R}$  reads

$$\boldsymbol{\nu}(\mathbf{v}_R) = \frac{1}{2} \varepsilon k_{iP} C_R \mathbf{v}_R^2, \quad (12)$$

solves Problem 1.

**Remark.** Under Assumption 1,  $\mathbf{v}^n - 3\Delta\mathbf{v} > 0$  holds, so that the interval in which  $\delta$  is to be selected is non empty.  $\lrcorner$

**Remark** (Interpretation of the proposed control law). Looking at (2b), it becomes apparent that the change of input variable  $\mathbf{d}_k \mapsto \mathbf{u}_k := \mathbf{v}_R \mathbf{d}_k$  (therefore, the choice of  $\mathbf{d}_k = \frac{1}{\mathbf{v}_R} \mathbf{u}_k$ ) makes the dynamics of  $\mathbf{i}_k$  linear. This also decouples the  $LC$  filter and grid models whose states are  $\boldsymbol{\eta}_k := [\mathbf{i}_k, \mathbf{v}_k, \mathbf{i}_{Gk}]^\top$  from the dynamics of  $\mathbf{v}_R$ .

The control law is designed in such a way that the dynamics of  $\boldsymbol{\eta}_k$  are fast compared to those of the integrators and reservoir voltage. The separation into the two timescales is performed by accelerating the dynamics of  $\boldsymbol{\eta}_k$  by adding a state-feedback  $\mathbf{u}_k = K\boldsymbol{\eta}_k + \dots$ , where  $K = [k_p, 0, 0]$ , and by slowing down the dynamics of  $\mathbf{z}_1, \dots, \mathbf{z}_{m-1}, \boldsymbol{\zeta}, \mathbf{v}_R$  using the gain  $\varepsilon$ .

The term  $\boldsymbol{\nu}(\mathbf{v}_R)$  is the energy in the reservoir capacitor multiplied by  $\varepsilon k_{iP}$ . Since its time-derivative is the sum of powers, it closely resembles the dynamics of the power integrators (11a), facilitating the proofs while achieving the exact regulation of  $\mathbf{v}_R$  since  $\boldsymbol{\zeta} = 0$  is equivalent to  $\mathbf{v}_R = \mathbf{v}_R^r$  under Fact 1.  $\lrcorner$

**Remark.** Prob. 1 is a general formulation in which the control law is a full state feedback (on  $\mathbf{v}_R, \mathbf{i}, \mathbf{v}$  and  $\mathbf{i}_G$ ). However, the proposed control law, given in Thm. 1 by (11) only depends on the measurements of  $\mathbf{v}_R$  and  $\mathbf{i}$ , both of which can be acquired locally through classical voltage and current sensors  $\lrcorner$

This section (Subsections 3.1 through 3.5) is dedicated to the proof of the theorem.

### 3.1. Existence of a closed-loop equilibrium point

**Lemma 2.** Select any  $(\theta, r) \in \mathcal{S}$  and consider the PFC model (2) in closed-loop with the control law (11). For this autonomous system, there exists a unique equilibrium  $(\mathbf{z}_1^*, \dots, \mathbf{z}_{m-1}^*, \boldsymbol{\zeta}^*, \mathbf{v}_R^*, \mathbf{i}^*, \mathbf{v}^*, \mathbf{i}_G^*)$  satisfying

$$\underline{\mathbf{v}} := \mathbf{v}^n - \Delta\mathbf{v} < \mathbf{v}_k^* < \mathbf{v}^n + \Delta\mathbf{v} =: \bar{\mathbf{v}}, \quad (k \in \llbracket 1, m \rrbracket).$$

This equilibrium reads:

$$\mathbf{z}_k^* = \mathbf{v}_k^* - k_p \mathbf{i}_k^* - \zeta^*, \quad (k \in \llbracket 1, m-1 \rrbracket), \quad (13a)$$

$$\zeta^* = \frac{1}{m} \sum_{k=1}^m (\mathbf{v}_k^* - k_p \mathbf{i}_k^*), \quad (13b)$$

$$\mathbf{v}_R^* = \mathbf{v}_R^r, \quad (13c)$$

$$\mathbf{i}_k^* = \mathbf{i}_{Gk}^* = \frac{1}{R_{Gk}} (V_{Gk} - \mathbf{v}_k^*), \quad (k \in \llbracket 1, m \rrbracket), \quad (13d)$$

$$\mathbf{v}_k^* = \frac{1}{2} \left( V_{Gk} + \sqrt{\Pi_k(\theta, r)} \right), \quad (k \in \llbracket 1, m \rrbracket). \quad (13e)$$

Furthermore, at this equilibrium, the reference is achieved, i.e. not only (13c) but also  $\mathbf{P}_k^* = \mathbf{P}_k^r$ , ( $k \in \llbracket 1, m-1 \rrbracket$ ) hold.

The proof can be found in Appendix B. Note that by definition of  $\Theta$ ,  $R_{Gk} \neq 0$ , and by Lemma 1,  $\Pi_k(\theta, r) > 0$ .

Before the stability of this point can be addressed, a change of state variables is performed.

### 3.2. Change of variables

Consider the change of state variables

$$T : \mathbb{R}^{4m+1} \rightarrow \mathbb{R}^{4m+1}$$

$$(\mathbf{z}_1, \dots, \mathbf{z}_{m-1}, \zeta, \mathbf{v}_R, \mathbf{i}, \mathbf{v}, \mathbf{i}_G) \mapsto (\psi_1, \dots, \psi_m, \zeta, \eta_1, \dots, \eta_m),$$

parametrised by the equilibrium given in Lem. 2, and defined by

$$\psi_k := \mathbf{z}_k - \mathbf{z}_k^* + \zeta - \zeta^*, \quad (k \in \llbracket 1, m-1 \rrbracket), \quad (14a)$$

$$\psi_m := \zeta - \zeta^* + \nu(\mathbf{v}_R) - \nu(\mathbf{v}_R^r) - \sum_{k=1}^{m-1} (\mathbf{z}_k - \mathbf{z}_k^*), \quad (14b)$$

$$\zeta := \zeta - \zeta^*, \quad (14c)$$

$$\eta_k := [\mathbf{i}_k, \mathbf{v}_k, \mathbf{i}_{Gk}]^\top - [\mathbf{i}_k^*, \mathbf{v}_k^*, \mathbf{i}_{Gk}^*]^\top, \quad (k \in \llbracket 1, m \rrbracket). \quad (14d)$$

where  $\nu$  is defined in (12). In the sequel, the elements of  $\eta_k$  are denoted  $[i_k, v_k, i_{Gk}]^\top$ . Let  $\mathcal{X}$  be the subset of  $\mathbb{R}^{4m+1}$  where the argument of  $T$  is such that  $\mathbf{v}_R > 0$ .

**Lemma 3.** *The restriction of the map  $T$  to  $\mathcal{X}$  is a diffeomorphism, and the PFC model (2) in closed-loop with the control law (11) can be written in the new coordinates as follows:*

$$\dot{x}(t) = \varepsilon f(x(t), \eta(t)), \quad (15a)$$

$$\dot{\eta}(t) = g(x(t), \eta(t)), \quad (15b)$$

where

$$x := [\psi_1, \dots, \psi_m, \zeta]^\top, \quad \eta := [\eta_1^\top, \dots, \eta_m^\top]^\top, \quad (16)$$

$$f(x, \eta) = \begin{bmatrix} k_{iP}((i_1 + \mathbf{i}_1^*)(k_p i_1 + \psi_1) + i_1 \mathbf{v}_1^*) \\ \quad + k_{iv}(-m\zeta + \sum_{k=1}^m \psi_k) \\ \quad \vdots \\ k_{iP}((i_m + \mathbf{i}_m^*)(k_p i_m + \psi_m) + i_m \mathbf{v}_m^*) \\ \quad + k_{iv}(-m\zeta + \sum_{k=1}^m \psi_k) \\ k_{iv}(-m\zeta + \sum_{k=1}^m \psi_k) \end{bmatrix}, \quad (17)$$

$$g(x, \eta) = \begin{bmatrix} A_1(\theta)\eta_1 + B\psi_1 \\ \quad \vdots \\ A_m(\theta)\eta_m + B\psi_m \end{bmatrix}, \quad B = \begin{bmatrix} \frac{-1}{L} \\ 0 \\ 0 \end{bmatrix}, \quad (18)$$

$$A_k(\theta) = \begin{bmatrix} \frac{-k_p}{C} & \frac{1}{L} & 0 \\ \frac{L_1}{C} & 0 & \frac{1}{C} \\ 0 & \frac{-1}{L_{Gk}} & -\frac{R_{Gk}}{L_{Gk}} \end{bmatrix}, \quad (k \in \llbracket 1, m \rrbracket). \quad (19)$$

*Proof.* See Appendix C.  $\square$

The system is now separated into a nonlinear subsystem (15a) and  $m$  independent linear subsystems whose states are  $\eta_k$ , governed by (15b). Note that the origin of (15) is an equilibrium, so that this change of variable is also a shift to error coordinates.

The stability of the origin of (15) is analysed along the *Singular Perturbations* method, well explained in (K.Khalil, 2002, p424); (15a) being the slow subsystem and (15b) being the fast one.

### 3.3. Stability of the fast dynamics

Take the system (15) and assume that  $\varepsilon = 0$ , hence that  $x$  is constant. The system then reduces to (15b) with  $x$  acting as a constant parameter, i.e.

$$\dot{\eta}(t) = g(x, \eta(t)). \quad (20)$$

**Proposition 1** (Fast dynamics). *For any  $(\theta, r) \in \mathcal{S}$  and any given constant  $x$ , the system (20) admits a globally exponentially stable equilibrium point  $\eta = h(x) = [h_1^\top(x), \dots, h_m^\top(x)]^\top$ , defined as*

$$h_k(x) := \left[ \frac{-1}{R_{Gk} + k_p}, \frac{R_{Gk}}{R_{Gk} + k_p}, \frac{-1}{R_{Gk} + k_p} \right]^\top \psi_k. \quad (21)$$

*Proof.* see Appendix D.  $\square$

### 3.4. Stability of the slow dynamics

Consider the change of time-variable  $t_s = \varepsilon t$ . The system (15) can be written in slow timescale:

$$\frac{d}{dt_s} x(t_s) = f(x(t_s), \eta(t_s)), \quad (22a)$$

$$\varepsilon \frac{d}{dt_s} \eta(t_s) = g(x(t_s), \eta(t_s)). \quad (22b)$$

Assume that  $\varepsilon = 0$ . This is equivalent to saying that  $\eta$  has already converged to its quasi-steady-state. This vector can then be replaced by  $h(x)$ , leading to the *reduced system*:

$$\frac{d}{dt_s} x(t_s) = f(x(t_s), h(x(t_s))). \quad (23)$$

**Proposition 2** (Slow dynamics). *Select  $k_{iv}$ ,  $\delta$  and  $k_{iP}$  as in Thm. 1. Pick any  $(\theta, r) \in \mathcal{S}$ . Then, the origin of system (23) is locally exponentially stable. Moreover, given*

$$\underline{\lambda} := \frac{\bar{R} + k_p}{R} (2\mathbf{v} - \bar{\mathbf{v}} - \delta), \quad (24)$$

the set

$$\mathcal{D} := \left\{ x \in \mathbb{R}^{m+1} : m\zeta^2 + \sum_{k=1}^m \psi_k^2 < \underline{\lambda}^2 \right\} \quad (25)$$

is included in the basin of attraction.

*Proof.* see Appendix E □

**Remark.** Note that since  $\bar{R} > 0$ ,  $k_p \geq 0$  and  $\delta < \mathbf{v}^n - 3\Delta\mathbf{v} = 2\mathbf{v} - \bar{\mathbf{v}}$ , it follows that  $\underline{\lambda} > 0$ . □

It has been proven that the slow and fast dynamics were stable in the case of an infinite timescale separation. The following subsection gives a proof of the stability of the whole system (slow and fast dynamics together) for non-infinite timescale separations.

### 3.5. Stability of the whole dynamics

Suppose now that  $\varepsilon > 0$ . Given any  $r, \rho \in \mathbb{R}_{>0}$ , define  $B_r := \{x \in \mathbb{R}^{m+1} : \|x\| < r\}$  and  $B_\rho(x) := \{\eta \in \mathbb{R}^{3m} : \|\eta - h(x)\| < \rho, (x \in B_r)\}$ . From the standard singular perturbations model (22), the following points can be verified for all  $(\theta, r) \in \mathcal{S}$ :

- $f(\mathbf{0}, \mathbf{0}) = \mathbf{0}$  and  $g(\mathbf{0}, \mathbf{0}) = \mathbf{0}$ .
- From Prop. 1, the equation  $g(x, \eta) = \mathbf{0}$  has a unique root  $\eta = h(x)$ , and  $h(\mathbf{0}) = \mathbf{0}$  for all  $x \in B_r$ .
- For all  $x \in B_r$  and  $\eta \in B_\rho$ , the functions  $f$ ,  $g$ ,  $h$  and their partial derivatives up to the second order are bounded because they are polynomials.
- The origin of the *reduced system*  $\frac{d}{dt_\varepsilon} x = f(x, h(x))$  is exponentially stable, according to Proposition 2.
- According to Proposition 1, the system  $\dot{\eta} = g(x, \eta)$  has a globally exponentially stable equilibrium point  $h(x)$ , uniformly in  $x$ . Then, the *Boundary-Layer system* can be written by selecting the change of coordinates  $\tilde{\eta} = \eta - h(x)$ , which gives  $\dot{\tilde{\eta}} = g(x, \tilde{\eta} + h(x))$ , whose origin is globally exponentially stable, uniformly in  $x$ .

Then, according to (K.Khalil, 2002, Thm. 11.4 p.456), there exists a  $\bar{\varepsilon} > 0$  such that for all  $0 < \varepsilon < \bar{\varepsilon}$ , the origin of (22) (and, equivalently, (15)) is exponentially stable.

Since  $T$  is a diffeomorphism on the domain of interest  $\mathcal{X}$  according to Lem. 3, the properties of stability can be propagated to the system in the original coordinates (2) in closed-loop with the control law (11). This concludes the proof of Theorem 1.

## 4. Comparison with prior studies

A new control law has been proposed though Thm. 1. In this section, a detailed comparison is given to the relevant published literature.

### 4.1. About (Ramirez et al., 2014)

This paper focuses on a two-terminal PFC, to which an additional branch (*third multiport*) has been added to compensate for the power losses inside the converter. Two control strategies have been proposed: a PI controller and a feedback linearisation controller. For the PI controller, current references are computed using the line voltages via  $\mathbf{i}_k^r(t) = \mathbf{P}_k^r / \mathbf{v}_k(t)$ , ( $k \in \{1, 2, 3\}$ ) where  $\mathbf{P}_2^r(t) = -\mathbf{P}_1^r(t)$  and  $\mathbf{P}_3^r(t) = \sum_{k=1}^3 \mathbf{i}_k^2(t) r_{Lk}$  is an estimation of the converter losses ( $r_{Lk}$  is the series resistance of the filter inductors). The duty cycles are then given by

$$\mathbf{d}_k(t) = -K_p(\mathbf{i}_k(t) - \mathbf{i}_k^r(t)) - K_i \int_0^t (\mathbf{i}_k(\tau) - \mathbf{i}_k^r(\tau)) d\tau.$$

The controller gains are computed using standard linear control techniques based on the linearisation of the system around an operation point. This approach is local, and the obtained stability certificate does not apply when the time dependency of the references  $i_k^r$  comes from that of the other state  $v_k$ . This last comment is even more critical when  $v_k$  (hence the reference  $i_k^r$ ) and the regulated current evolve with similar dynamics, which is the case here (see Fig. 6 (b)&(c)). The second control law uses the same current references, but the duty cycles are computed via an approximate feedback linearisation:

$$\mathbf{d}_k(t) = \frac{1}{\mathbf{v}_R(t)} \left[ \mathbf{v}_k(t) - r_{Lk} \mathbf{i}_k(t) - L_k \frac{d\mathbf{i}_k^r(t)}{dt} \right] + \frac{\gamma_k}{\mathbf{v}_R(t)} L_k (\mathbf{i}_k(t) - \mathbf{i}_k^r(t)),$$

where  $L_k$  are the filter inductors and  $\gamma_k$  are tuning gains. This latter technique suffers from measurement noise due to the derivative term, and requires a differentiation filter for which no proof is given. It is said in the paper that this control strategy leads to exponentially converging dynamics, but only the dynamics of the current are analysed separately, this is not proven for the reservoir voltage. In both of these strategies, steady-state errors remain on the power objectives. The idea of estimating the converter losses instead of including a feedback loop on the reservoir voltage measurement is fragile in essence because not all losses can be modelled, and would necessarily lead to a drift in the reservoir voltage. To overcome this limitation, a proposition has been made in the last part of the paper involving an outer PI loop on the tracking error of the reservoir voltage. Another proposition involved the addition of a branch connected to a battery and fully dedicated to the control of the reservoir voltage. Both of these suggestions are heuristic. The first one is said to bring marginal improvements, while the second achieves

a better performance, at the cost of an extra converter branch. These methods seem generalisable to more than two terminals, although this claim should be tested. They both require  $2m + 1$  measurements.

#### 4.2. About (Natori et al., 2018)

This paper focuses on a two-terminal PFC. It aims to improve a previous study (Takahashi et al., 2015) by removing an additional branch (*compensation node*) that had been added to cope with the fluctuations in the reservoir voltage due to power imbalances in the converter. For each branch, the proposed control strategy is the following: A current reference is computed using the voltage at the other end of the line:  $\mathbf{i}_k^r = \mathbf{P}_k^r / V_{Gk}$ . The duty cycle is then computed using the relation

$$\mathbf{d}_k = \frac{1}{\mathbf{v}_R} \left( \mathbf{v}_k - K_p(\mathbf{i}_k - \mathbf{i}_k^r) - K_i \int (\mathbf{i}_k - \mathbf{i}_k^r) \right).$$

As shown in the paper, this strategy effectively makes the fluctuations of the power in the lines independent from that of the reservoir voltage thanks to the term  $\frac{1}{\mathbf{v}_R}$ . However, the opposite is not true. As shown in (2a), the dynamics of the reservoir voltage depend on the duty cycle and the current in each branch. No control strategy is proposed for the regulation of  $\mathbf{v}_R$ . During the experiments, this voltage has been controlled by an external power supply, suggesting that it may drift outside acceptable boundaries in practice. Moreover, the definition of the current reference depends on a non-local information,  $V_{Gk}$ . The analysis of stability is merely performed on a scalar linear time invariant system representing the dynamics of the filter inductors, a highly simplified model in comparison to the model given in (2). It seems generalisable to more than two terminals, although this should be tested. It requires  $2m + 1$  measurements.

#### 4.3. About (Simon et al., 2021a)

This paper is the authors' first control law for a three-terminal PFC. In this paper, the model (2) is offered. To this model, three integrators are added, respectively on the error on the two first powers  $\mathbf{P}_k - \mathbf{P}_k^r$ , ( $k \in \{1, 2\}$ ) and the error on the reservoir voltage  $\mathbf{v}_R - \mathbf{v}_R^r$ . The model is augmented with these integrators, linearised and a full state feedback controller is derived:

$$\mathbf{d} = K_p \mathbf{x} + K_i \mathbf{z} + \mathbf{d}_{FF},$$

where  $\mathbf{x}$  is the vector of every state of the system (according to model (2)),  $\mathbf{z}$  is the vector of integrators and  $\mathbf{d}_{FF}$  is a constant feedforward term. This control law is the first one to truly obtain a regulation of the reservoir voltage as well as a regulation of all the power references without any additional branch. It achieves local asymptotic stability of the equilibrium and local robustness properties with regard to the uncertain model parameters. Limited instructions are given to choose the poles of the system. This strategy is generalisable to  $m$  terminals, but requires  $3m + 1$  measurements.

#### 4.4. About (Lin-Shi et al., 2021)

In this paper, another controller is derived based on flatness techniques. The resulting controller is composed of feedback linearising terms (*inverse dynamics*) followed by nested PI tracking loops. Local proofs of stability can be deduced from flatness theory, but these depend on a simplified version of the model (2) in which the uncertainty of the grid does not appear. The use of feedback linearising terms is also fragile to model uncertainties, especially since all terms including the stabilising ones are cancelled in the dynamics. A tuning procedure is given for the control gains. It does not require explicit knowledge of the grid, but may depend implicitly on its uncertainties. This technique is designed for an arbitrary number  $m$  of terminals and requires  $2m + 1$  measurements.

#### 4.5. About (Simon et al., 2021a)

This last paper proposes a new control law for the PFC based on Forwarding techniques. The model (2) is used, and a nonlinear (polynomial) control law is derived. It achieves semi-global stability of the equilibrium in the state-space. This implies that for each subset of initial conditions in the state-space  $\mathcal{X}$ , it is shown how to tune the control law to create an equilibrium which is asymptotically stable and whose basin of attraction contains the given subset  $\mathcal{X}$  of the state-space. Furthermore, this stability is local in the parametric space. This means that, in the parametric space, there exists a neighbourhood  $\hat{\mathcal{S}}$  of the nominal parameters where the existence of the equilibrium is guaranteed together with its asymptotic stability. An important limitation of this paper is the lack of proof of stability for every uncertain parameter in  $\mathcal{S}$ :  $\hat{\mathcal{S}}$  may be very small compared to the required set  $\mathcal{S}$ . Limited instructions are given to tune the gains, and the law is implemented based on the knowledge of some nominal parameters of the grid. The control law is generalisable to  $m$  terminals, but requires a full state feedback:  $3m + 1$  measurements.

#### 4.6. Comparison with the new control law

The major improvement brought by the control law proposed in this paper is the proof of existence and asymptotic stability of the equilibrium for every parameter in  $\mathcal{S}$ , based on a realistic model of the system. This enables to capture the high uncertainty of the grid, and facilitates the implementation of the control law. Indeed, the law does not require any knowledge of the grid other than the maximum possible resistance  $R_{Gk}$ . Moreover, this control law is designed for an arbitrary number  $m$  of branches and requires only  $m + 1$  measurements. Three gains ( $k_p, k_{iP}, k_{iv}$ ) have to be tuned via a precise method, allowing for a rapid practical implementation, illustrated in the following section.

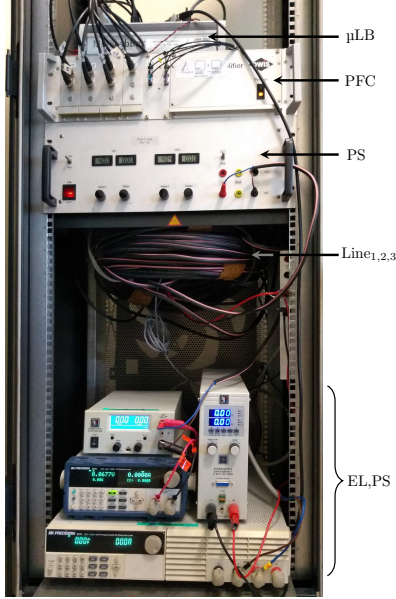


Figure 4: Picture of the experimental set-up

## 5. Experimentations

The experiments are lead on a 3-terminal PFC ( $m = 3$ ). The experimental set-up is first described, before showing how Thm. 1 can be applied in practice and presenting the results.

### 5.1. Experimental set-up

The experimental set-up is presented on Fig. 4 and 5, where the PFC corresponds to the circuit of Fig. 2. A dSPACE MicroLabBox rapid prototyping system (noted by  $\mu\text{LB}$  in Fig. 4&5) is programmed with the control law and generates the gate signals for the IGBTs of the PFC. For each line (marked by a black rectangle), thirty meters of standard U1000 RV2 cable are used to approach real conditions testing. The first line is connected to a load made of a resistor in series with an electronic load (noted by EL-R)<sup>2</sup>. The second line is connected to a bus on which a power supply (PS) and an electronic load (EL) are connected to allow for bidirectional power flows. The third line is connected to a power supply (noted PS). Note that all power supplies and electronic loads are voltage regulated with the values  $V_{Gk}$  in Tab. 2.

### 5.2. Practical implementation and tuning of the control parameters

*Practical expression of the control law.* Following Thm. 1, the control law to be applied to the system is the following,

<sup>2</sup>The resistor is not visible on Fig. 4 due to a lack of space. It is a high power wire wound resistor.

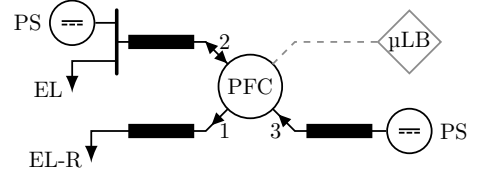


Figure 5: Drawing of the experimental set-up

where  $\mathbf{v}_R(t)$ ,  $\mathbf{i}_1(t)$ ,  $\mathbf{i}_2(t)$  and  $\mathbf{i}_3(t)$  are measured:

$$\mathbf{d}_1(t) = \frac{1}{\mathbf{v}_R(t)} (k_p \mathbf{i}_1(t) + \mathbf{z}_1(t) + \zeta(t)), \quad (26a)$$

$$\mathbf{d}_2(t) = \frac{1}{\mathbf{v}_R(t)} (k_p \mathbf{i}_2(t) + \mathbf{z}_2(t) + \zeta(t)), \quad (26b)$$

$$\mathbf{d}_3(t) = \frac{1}{\mathbf{v}_R(t)} \left( k_p \mathbf{i}_3(t) + \varepsilon \frac{1}{2} k_{iP} C_R (\mathbf{v}_R(t)^2 - (\mathbf{v}_R^r)^2) - \mathbf{z}_1(t) - \mathbf{z}_2(t) + \zeta(t) \right); \quad (26c)$$

And the integrators are updated using the following law:

$$\dot{\mathbf{z}}_1(t) = \varepsilon k_{iP} (\mathbf{i}_1(t) \mathbf{v}_R(t) \mathbf{d}_1(t) - \mathbf{P}_1^r), \quad (26d)$$

$$\dot{\mathbf{z}}_2(t) = \varepsilon k_{iP} (\mathbf{i}_2(t) \mathbf{v}_R(t) \mathbf{d}_2(t) - \mathbf{P}_2^r), \quad (26e)$$

$$\dot{\zeta}(t) = \frac{1}{2} \varepsilon^2 k_{iv} k_{iP} C_R (\mathbf{v}_R(t)^2 - (\mathbf{v}_R^r)^2). \quad (26f)$$

*Selection of  $\delta$ .* The test bench used for these experiments is rated at a tenth scale: The value  $\mathbf{v}^n = 40$  V has been selected. A voltage tolerance of  $\Delta \mathbf{v} = 5\%$  is assumed, i.e.  $\underline{\mathbf{v}} = 38$  V and  $\bar{\mathbf{v}} = 42$  V. In Thm. 1,  $\delta$  must therefore be chosen smaller than  $\mathbf{v}^n - 3\Delta \mathbf{v} = 34$  V. Remark from the statement of the theorem that a small  $\delta$  leads to  $k_{iv} \ll k_{iP}$ , hence a very slow regulation of  $\mathbf{v}_R$  compared to  $\mathbf{P}_k$ , see (26d)-(26f). Remark also from (24) and (25) that a large  $\delta$  leads to a small basin of attraction  $\mathcal{D}$  for the slow subsystem. It appears that there is a trade-off between the dynamic of  $\mathbf{v}_R$  and the size of the basin of attraction. For these experiments, the middle value is taken, i.e.  $\delta = 17$  V.

*Selection of the controller gains.* Assume that the maximum resistance  $\bar{R}$  on this tenth-scale system is of  $50\Omega$ . In comparison, the maximum value in the current set-up is  $R_{G1} = 21.7 \Omega$  (see Tab. 2). For  $k_p = 2 \Omega$ , it follows that  $l(\delta) = \frac{\delta}{\bar{R} + k_p} = 17/52 \approx 0.33$  A. Recall that  $\mathbf{v}_R$  is an internal voltage in the converter which should simply be maintained within a certain range, the main objective being the power regulation. Using the value of  $l(\delta)$  above, the theorem states that  $k_{iP}$  should be greater than  $mk_{iv}/l(\delta) \approx 9k_{iv}$ . It is clear that this choice of gains complies with the control priorities. After temporarily choosing  $\varepsilon = 1$  and running precise simulations, the values  $k_{iv} = 10$ , and therefore  $k_{iP} = 100$  gave satisfactory results. Unless otherwise stated, these values are the ones used in the following experiments and simulations.

The control law can be applied to the experimental set-up for a small  $\varepsilon$ , increasing it until the required speed is reached. An estimate of  $\bar{\varepsilon}$  can be found empirically, as shown later.

### 5.3. Robust Regulation

The results of the first experiment are displayed in Fig. 6. At  $t = 0$  s, the closed-loop system is at a steady-state on a set-point described by  $\theta$  in Tab. 2 and  $r = [\mathbf{P}_1, \mathbf{P}_2, \mathbf{v}_R]^T = [-70 \text{ W}, 75 \text{ W}, 55 \text{ V}]^T$ .

Initially, the load on the first line is entirely supplied by the second line, while the third is idled ( $\mathbf{P}_3 \approx 0 \text{ W}$ ). Recall that the generator convention is used, so supplying lines have a positive power. Recall also that only the  $m - 1 = 2$  first lines have a power reference, allowing the last one to naturally converge to the overall power balance:  $-\mathbf{P}_1^r - \mathbf{P}_2^r$  plus the power losses in the converter.

At  $t = 15$  ms, a large step is applied on the second power reference, changing  $\mathbf{P}_2^r$  from 75 W to  $-100$  W. Since the power dynamics are much faster than the reservoir voltage dynamics (because  $k_{iP} = 10k_{iv}$ ), the power, current and voltage transient are displayed in a zoomed graph. The second line becomes a load while it was acting as a source, the third line supplies the total power to the two first ones and the first line sees little perturbation from this switch. Moreover, observe on Fig. 7 that the duty cycles do not saturate during this event. The reservoir voltage falls by 1.5 V (2.7 %). Recall that this voltage is internal to the converter, which means it does not require a tight regulation, as long as it does not exceed its boundaries. As shown with the next event, this slow regulation allows better transients for the foremost control objectives  $\mathbf{P}_1^r$  and  $\mathbf{P}_2^r$ .

At  $t = 120$  ms, a voltage step is provoked with the electronic load on the first line, changing  $V_{G1}$  from 1.6 V to 8.5 V. The regulation of the first power is properly managed, and the fact that  $k_{iP} = 10k_{iv}$  allows the reservoir voltage to act as an energy buffer that minimises the propagation of this perturbation to the other lines. Indeed, the reservoir experiences a larger overshoot (13 %). However, observe on Fig. 7 that, due to the terms  $1/\mathbf{v}_R$  in (26), the duty cycles properly compensate for this overshoot, hereby limiting its effect to the other lines.

Eventually, at  $t = 250$  ms, the reservoir voltage reference is increased, changing  $\mathbf{v}_R^r$  from 55 V to 60 V. It can be observed in Fig. 6(d)-(f) that some energy is taken from the lines to charge the reservoir capacitor. Since this effort is shared between all the lines and since the capacitor is quite small (60  $\mu\text{F}$ ), this perturbation is quickly handled.

Note that the set-points for this experiment have been chosen near the boundaries of  $\mathcal{S}$ : On Fig. 6(c), the line voltages jump from one extreme value to the other ( $\mathbf{v}_k^* \in ]38, 42[ \text{ V}$ ), illustrating the robustness of the proposed control method. Remark that the overshoots are both short and of small magnitude.

Remark also in Fig. 6(b) that the currents are well controlled, with  $\mathbf{i}_2$  switching from 2 A to  $-2$  A with little to no overshoot.

### 5.4. Estimation of $\bar{\varepsilon}$

In the Sec. 5.3, the results are obtained for  $\varepsilon = 1$ . In this sub-section, the power step on  $\mathbf{P}_2^r$  that was performed

Table 2: Experiment numerical values

	Parameter	Initial value			Unit
		$k = 1$	$k = 2$	$k = 3$	
$\theta$	$L_{Gk}$	18	18	18	$\mu\text{H}$
	$R_{Gk}$	21.7	1.30	1.23	$\Omega$
	$V_{Gk}$	1.6	40	42	V
$L$	750 mH	$C$	20 $\mu\text{F}$	$C_R$	60 $\mu\text{F}$
$t_{dead-time}$	0.3 $\mu\text{s}$	$F_{SW}$	15 kHz	$\tau_L$	1 $\Omega$

at  $t = 15$  ms is reproduced for different values of  $\varepsilon$ , and displayed in Fig. 8. It can be seen that smaller values of  $\varepsilon$  lead to slower dynamics, while larger values lead to an oscillation of the power as the slow subsystem begins to interact with the fast one. Even larger values lead to the instability of the system. It appears that  $\varepsilon = 1$  is an appropriate choice for this system and these control gains, and that  $\bar{\varepsilon}$  can be assumed greater than 2.5 for the value of  $(\theta, r)$  imposed at  $t = 15$  ms.

### 5.5. Estimation of the Basin of Attraction

The estimation of the basin of attraction of the closed-loop system is a complex task because it is nonlinear with  $3m = 9$  uncertain parameters and  $n + m = 4m + 1 = 13$  states. It is however possible to grasp an idea of its geometry through stochastic simulations:

First, select a set-point  $(\theta, r) \in \mathcal{S} \subset \Theta \times \mathcal{R}$  using a random uniform law. Note that in addition to the constraints defined in  $\mathcal{R}$ ,  $\Theta$  and  $\mathcal{S}$ , other bounds must be defined on  $L_{Gk}$ ,  $\mathbf{P}_k$  and  $\mathbf{i}_k$  to exclude unrealistic set-points. Compute the single equilibrium point associated with  $(\theta, r)$  in  $\mathcal{E}(\theta, r)$  using (13).

Second, select initial line voltages and an initial reservoir voltage. The full basin of attraction lies in a 13-dimensional space which cannot be graphed. Hence, only the influence of different initial conditions on the first line and on  $\mathbf{v}_R$  will be studied.  $\mathbf{v}_1$  and  $\mathbf{v}_R$  are selected using a random uniform law, in the intervals  $[0, 60]$  V and  $[40, 100]$  V, respectively. To reduce the impact of the initial conditions of the other lines,  $\mathbf{v}_2$  and  $\mathbf{v}_3$  are initialised on their equilibrium value:  $\mathbf{v}_k(0) = \mathbf{v}_k^* = \frac{1}{2} \left( V_{Gk} + \sqrt{\Pi_k(\theta, r)} \right)$ , ( $k \in \llbracket 2, 3 \rrbracket$ ). Compute the steady-state initial conditions for the currents and the integrators using

$$\begin{aligned} \mathbf{i}_k(0) &= \mathbf{i}_{Gk}(0) = (V_{Gk} - \mathbf{v}_k(0))/R_{Gk}, (k \in \llbracket 1, 3 \rrbracket), \\ \zeta(0) &= \frac{1}{3} \sum_{k=1}^3 (\mathbf{v}_k(0) - k_p \mathbf{i}_k(0)), \\ \mathbf{z}_k(0) &= \mathbf{v}_k(0) - k_p \mathbf{i}_k(0) - \zeta(0), (k \in \llbracket 1, 2 \rrbracket). \end{aligned}$$

Initial conditions yielding duty cycles above 1 or currents outside  $[-20, 20]$  A are excluded.

Third, simulate the averaged model (2) in closed-loop with the controller (26) tuned as in Sec. 5.2 with the set-

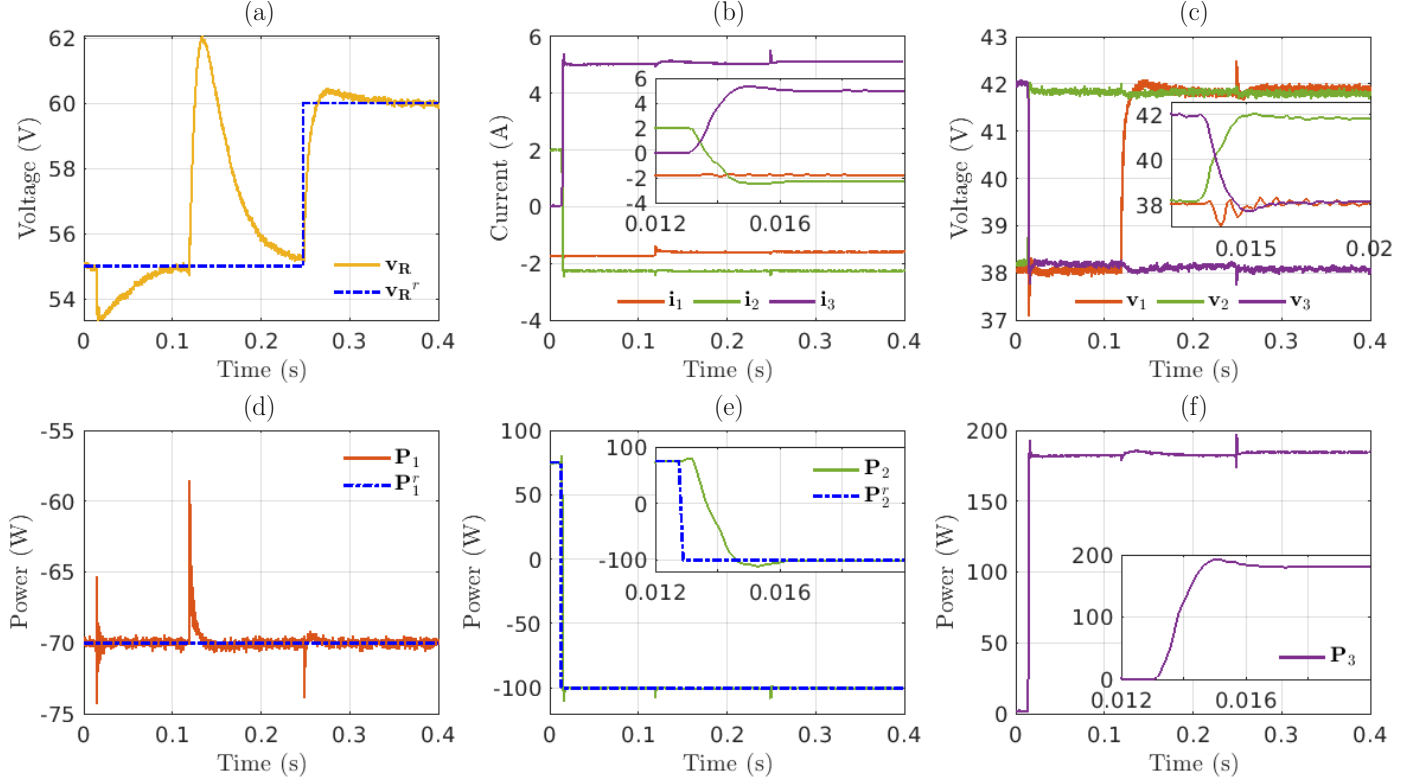


Figure 6: Experimental measurements of (a) the reservoir voltage with its reference, (b) the inductor currents, (c) the line voltages and (d)-(f) the power in each line with their references during the experiment of Sec. 5.3. The inner sub-figures are time-zooms between 12 and 18 ms to exhibit transients, and the references are graphed in dashed-dotted blue lines.

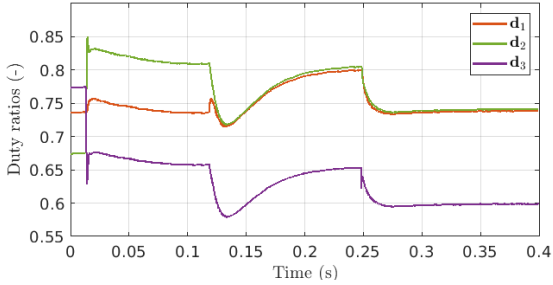


Figure 7: Experimental recording of the duty ratios during the experiment of Sec. 5.3

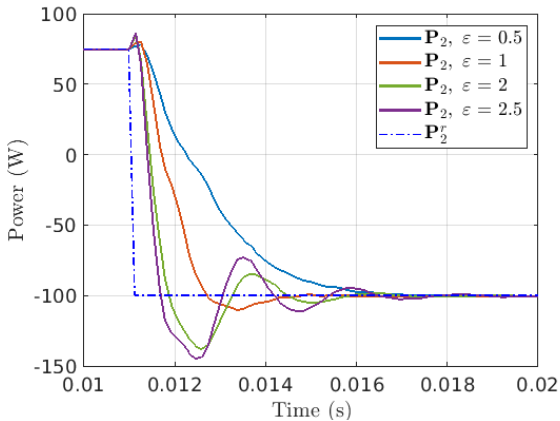


Figure 8: Experimental measurements of the tracking dynamics of  $P_2$  for different values of  $\epsilon$

point  $(\theta, r)$  and the new initial conditions. Stop the simulation if one of the states exceeds a given unrealistic value.

Eventually, repeat the second and third steps for multiple initial conditions and repeat the whole algorithm for multiple set-points.

Note beforehand that for a given steady-state line voltage, the line power can be expressed as  $\mathbf{P}_k^* = -\frac{1}{R_{Gk}}(\mathbf{v}_k^*)^2 + \frac{V_{Gk}}{R_{Gk}}\mathbf{v}_k^*$ . Its graph is the inverted parabola drawn in thin grey lines in Fig. 9&10. Fig. 9 is obtained through experimental measurements. A single set-point (and equilibrium) is tested, along with four steady-state initial conditions around it, corresponding to the constant duty cycles  $\mathbf{d}(0) = \{0.6 \times \mathbf{1}_3, 0.7 \times \mathbf{1}_3, 0.8 \times \mathbf{1}_3, 0.9 \times \mathbf{1}_3\}$ . The measured trajectories of the closed-loop system are projected in the  $\mathbf{v}_2 - \mathbf{P}_2$  plane.

The experimentations of Fig. 9 are reproduced numerically with the averaged model simulations for five set-points and one thousand initial conditions each in Fig. 10. The trajectories of the states between the initial conditions and the equilibrium are omitted for clarity. The required bounds on the line voltage  $\underline{\mathbf{v}}, \bar{\mathbf{v}}$  are illustrated by the two vertical lines.

The portions of the steady-state power parabolas for which no point is drawn yielded excessively high initial currents ( $\mathbf{i}_k(0) > 20$  A) and were left out. No unstable initial conditions have been found in these five thousand simulations, despite the fact that some initial points have

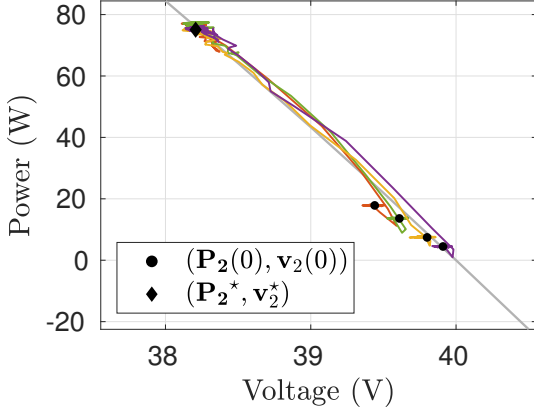


Figure 9: Experimental measurements of the trajectories of the closed-loop system projected in the  $\mathbf{v}_2 - \mathbf{P}_2$  plane for one equilibrium point and different initial conditions (corresponding to the constant duty cycles  $\mathbf{d}(0) = \{0.6 \times \mathbf{1}_3, 0.7 \times \mathbf{1}_3, 0.8 \times \mathbf{1}_3, 0.9 \times \mathbf{1}_3\}$ ). The thin grey line is the steady-state power as a function of the steady-state line voltage. Each trajectory is plotted in a different colour.

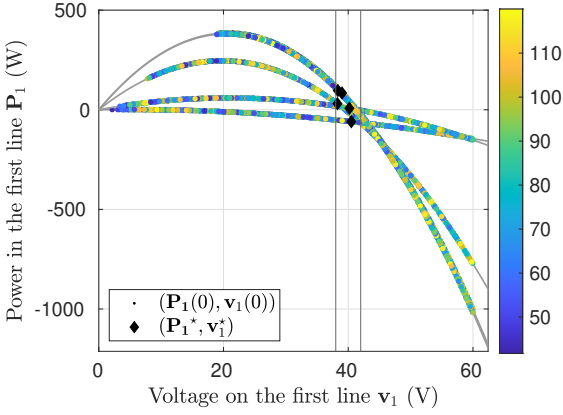


Figure 10: Simulated stable initial conditions of the closed-loop system for five random set-points in  $\mathcal{S}$  projected in the  $\mathbf{v}_1 - \mathbf{P}_1$  plane. The two vertical lines indicate  $\underline{\mathbf{v}}$  and  $\bar{\mathbf{v}}$ , and the grey lines are the steady-state power associated with each set-point as a function of the steady-state line voltage. The color bar indicates the initial reservoir voltage  $\mathbf{v}_{\mathbf{R}}(0)$  in volts.

been taken very far from their equilibrium value. Note also that the power parabolas associated with each set-point are very different, showing that the proposed control law is robust to large parametric uncertainties. Changing  $\theta$  affects the coefficients of the parabola. Changing  $r$  results in sliding the diamond on the parabola, while remaining within the two vertical lines (i.e.  $\underline{\mathbf{v}} < \mathbf{v}_k^* < \bar{\mathbf{v}}$ ) and below the grey curve's maximum (i.e.  $\mathbf{P}_k^* = \mathbf{P}_k^r < \mathbf{P}_{k,max} := V_{Gk}^2 / 4R_{Gk}$ , which is equivalent to  $\Pi_k(\theta, r) > 0$ ).

## 6. Conclusion

This paper proposed a new control law for a low voltage DC PFC. The proofs of stability ensure a robustness to any relevant grid parameters along the chosen model: it is proven that for any of these relevant grid parameters,

there exists an equilibrium on which the control objectives are met, and that this equilibrium remains asymptotically stable. The necessary measurements are limited to one current per branch and one voltage inside the converter, and are all *local* measurements. The tuning of the control gains is intuitive and aided by the main theorem. The control law only requires the knowledge of the maximum possible resistance in the grid. This new control law has been compared to the relevant literature, illustrating notable improvements in the given proofs of stability and robustness, as well as practical advantages such as the limited number of required measurements (and sensors) and the tuning procedure for the control gains. As shown by the experimental measurements, this method yields good results concerning both the speed of the regulation and its robustness to load and reference steps. A needed improvement to this method is the addition of formal guarantees with regard to the initial conditions. This may be achieved using (Saber and Khalil, 1984). However, the experimental results and stochastic simulations presented in the paper suggest that the basin of attraction may be sufficiently large for a practical implementation. Future studies will involve the adaptation of existing secondary-level grid control algorithms to define the power and reservoir voltage references to be tracked.

## Appendix A. Proof of Lemma 1

The first step is to obtain a characterisation of  $\mathcal{E}$ , which is given as

$$\mathcal{E}(\theta, r) = \left\{ (\mathbf{v}_{\mathbf{R}}^*, \mathbf{i}^*, \mathbf{v}^*, \mathbf{i}_{\mathbf{G}}^*, \mathbf{d}^*) \text{ s.t.} \right.$$

$$\mathbf{v}_{\mathbf{R}}^* = \mathbf{v}_{\mathbf{R}}^r, \quad (\text{A.1a})$$

$$\mathbf{i}_k^* = \frac{1}{R_{Gk}} (V_{Gk} - \mathbf{v}_k^*), \quad (\text{A.1b})$$

$$\mathbf{v}_k^* = \frac{1}{2} \left( V_{Gk} + \sqrt{\Pi_k(\theta, r)} \right), \quad (\text{A.1c})$$

$$\mathbf{i}_{\mathbf{G}k}^* = \mathbf{i}_k^*, \quad (\text{A.1d})$$

$$\mathbf{d}_k^* = \frac{\mathbf{v}_k^*}{\mathbf{v}_{\mathbf{R}}^r}, \quad (k \in \llbracket 1, m \rrbracket) \left. \right\}, \quad (\text{A.1e})$$

where  $\mathbf{v}_{\mathbf{R}}^r > 0$  by definition of  $\mathcal{R}$ . This statement is proven as follows: Consider the model (2). By writing (2a) to (2d) = 0 and  $\mathbf{v}_{\mathbf{R}}^* = \mathbf{v}_{\mathbf{R}}^r$ ,  $\mathbf{P}_k^* = \mathbf{P}_k^r$ , the following set of equations is found

$$\left\{ \begin{array}{l} \sum_{k=1}^m \mathbf{i}_k^* \mathbf{d}_k^* = 0, \end{array} \right. \quad (\text{A.2a})$$

$$\left\{ \begin{array}{l} \mathbf{v}_k^* - \mathbf{v}_{\mathbf{R}}^* \mathbf{d}_k^* = 0, \end{array} \right. \quad (\text{A.2b})$$

$$\left\{ \begin{array}{l} \mathbf{i}_{\mathbf{G}k}^* - \mathbf{i}_k^* = 0, \end{array} \right. \quad (\text{A.2c})$$

$$\left\{ \begin{array}{l} V_{Gk} - \mathbf{v}_k^* - R_{Gk} \mathbf{i}_{\mathbf{G}k}^* = 0, \end{array} \right. \quad (\text{A.2d})$$

where  $k \in \llbracket 1, m \rrbracket$ , and

$$\left\{ \begin{array}{l} \mathbf{P}_k^* = \mathbf{i}_k^* \mathbf{v}_{\mathbf{R}}^* \mathbf{d}_k^* = \mathbf{P}_k^r, \end{array} \right. \quad (k \in \llbracket 1, m-1 \rrbracket) \quad (\text{A.3a})$$

$$\left\{ \begin{array}{l} \mathbf{v}_{\mathbf{R}}^* = \mathbf{v}_{\mathbf{R}}^r. \end{array} \right. \quad (\text{A.3b})$$

Solving (A.2b) and (A.2c) results in

$$\mathbf{d}_k^* = \frac{\mathbf{v}_k^*}{\mathbf{v}_R^*} \quad \text{and} \quad \mathbf{i}_k^* = \mathbf{i}_{Gk}^*. \quad (\text{A.4})$$

(A.2a) can be re-written as

$$\frac{1}{\mathbf{v}_R^*} \sum_{k=1}^m \mathbf{i}_k^* \mathbf{v}_R^* \mathbf{d}_k^* = 0, \quad (\text{A.5})$$

where  $\mathbf{v}_R^* = \mathbf{v}_R^r > 0$  by (A.3b) and the definition of  $\mathcal{R}$ . Taking (A.3a) in (A.5) results in

$$\frac{1}{\mathbf{v}_R^*} \left( \sum_{k=1}^{m-1} \mathbf{P}_k^r + \mathbf{i}_m^* \mathbf{v}_R^* \mathbf{d}_m^* \right) = 0, \quad (\text{A.6})$$

hence,  $\mathbf{i}_m^* \mathbf{v}_R^* \mathbf{d}_m^* = -\sum_{k=1}^{m-1} \mathbf{P}_k^r \stackrel{(\text{7})}{=} \mathbf{P}_m^r$ . Using (A.2d) and (A.4), the equilibrium currents can be found:

$$\mathbf{i}_k^* = \mathbf{i}_{Gk}^* = \frac{1}{R_{Gk}} (V_{Gk} - \mathbf{v}_k^*). \quad (\text{A.7})$$

Then, multiplying (A.7) by  $R_{Gk} \mathbf{v}_k^*$  and using (A.3a) (recall that  $\mathbf{v}_R^* \mathbf{d}_k^* = \mathbf{v}_k^*$ ), it follows that

$$-(\mathbf{v}_k^*)^2 + V_{Gk} \mathbf{v}_k^* - R_{Gk} \mathbf{P}_k^r = 0. \quad (\text{A.8})$$

Assume that  $\Pi_k(\theta, r) \stackrel{(6)}{=} V_{Gk}^2 - 4R_{Gk} \mathbf{P}_k^r \geq 0$ . The solutions to (A.8) are then

$$\mathbf{v}_k^* = \frac{1}{2} \left( V_{Gk} \pm \sqrt{\Pi_k(\theta, r)} \right). \quad (\text{A.9})$$

The line voltage constraints should now be taken into account to complete the characterisation of  $\mathcal{E}$ .

Remember that from the definition of  $\Theta$ ,  $V_{Gk} \leq \bar{\mathbf{v}}$ . Since  $\mathbf{v}^n > 3\Delta \mathbf{v}$  by Assumption 1, then  $\frac{1}{2}\bar{\mathbf{v}} < \underline{\mathbf{v}}$  and it results that  $\frac{1}{2} \left( V_{Gk} - \sqrt{\Pi_k(\theta, r)} \right) \leq \frac{1}{2} V_{Gk} < \underline{\mathbf{v}}$ . Therefore, only  $\mathbf{v}_k^* = \frac{1}{2} \left( V_{Gk} + \sqrt{\Pi_k(\theta, r)} \right)$  can possibly be contained in the  $]\underline{\mathbf{v}}, \bar{\mathbf{v}}[$  interval. It also follows from this discussion that the voltage bounds cannot be satisfied if  $\Pi_k(\theta, r) = 0$ . This concludes the characterisation of  $\mathcal{E}$ .

From these steps, it appears that  $\mathcal{E}$  is non-empty for every  $(\theta, r) \in \Theta \times \mathcal{R}$  such that

$$\Pi_k(\theta, r) = V_{Gk}^2 - 4R_{Gk} \mathbf{P}_k^r > 0 \quad (\text{A.10})$$

and

$$\underline{\mathbf{v}} < \frac{1}{2} \left( V_{Gk} + \sqrt{\Pi_k(\theta, r)} \right) < \bar{\mathbf{v}}, \quad (\text{A.11})$$

for all  $k$ . This completes the characterisation of  $\mathcal{S}$ .

## Appendix B. Proof of Lemma 2

Equating to zero the derivatives of the dynamical part of the controller gives:

$$0 = \varepsilon k_{iP} (\mathbf{P}_k^* - \mathbf{P}_k^r), \quad (k \in \llbracket 1, m-1 \rrbracket), \quad (\text{B.1})$$

$$0 = \varepsilon k_{iv} (\boldsymbol{\nu}(\mathbf{v}_R^*) - \boldsymbol{\nu}(\mathbf{v}_R^r)). \quad (\text{B.2})$$

Bearing in mind the definition of  $\boldsymbol{\nu}$  given by (12), and the fact that  $\varepsilon$ ,  $k_{iv}$ ,  $k_{iP}$  and  $C_R$  are strictly positive constants, (B.1) implies  $\mathbf{P}_k^* = \mathbf{P}_k^r$ , ( $k \in \llbracket 1, m-1 \rrbracket$ ) and (B.2) leads to  $\mathbf{v}_R^* = \pm \mathbf{v}_R^r$ . Physical considerations, formalized via Fact 1, prove that  $\mathbf{v}_R^* = \mathbf{v}_R^r$ .

As a result, if there exists a closed-loop equilibrium such that  $\underline{\mathbf{v}} < \mathbf{v}_k^* < \bar{\mathbf{v}}$ , ( $k \in \llbracket 1, m \rrbracket$ ), then it satisfies  $(\mathbf{v}_R^*, \mathbf{i}^*, \mathbf{v}^*, \mathbf{i}_G^*, \mathbf{d}^*) \in \mathcal{E}(\theta, r)$  for some  $\mathbf{d}^*$ . In such a case, Lem. 1 proves that  $(\mathbf{v}_R^*, \mathbf{i}^*, \mathbf{v}^*, \mathbf{i}_G^*, \mathbf{d}^*)$  is unique and that (A.1a), (A.1b), (A.1c), (A.1d) and  $\mathbf{d}_k^* = \mathbf{v}_k^*/\mathbf{v}_R^*$  hold, see (A.1e). Thus, it remains to show that  $\mathbf{d}_k^*$  equals  $\mathbf{v}_k^*/\mathbf{v}_R^*$  for a unique  $\mathbf{z}^*$  and  $\boldsymbol{\zeta}^*$ . This is achieved by writing (11c) and (11d) at the equilibrium, i.e.

$$\frac{\mathbf{v}_k^*}{\mathbf{v}_R^*} = \frac{1}{\mathbf{v}_R^*} (k_p \mathbf{i}_k^* + \mathbf{z}_k^* + \boldsymbol{\zeta}^*), \quad (k \in \llbracket 1, m-1 \rrbracket), \quad (\text{B.3})$$

$$\frac{\mathbf{v}_m^*}{\mathbf{v}_R^*} = \frac{1}{\mathbf{v}_R^*} \left( k_p \mathbf{i}_m^* + \boldsymbol{\zeta}^* + \boldsymbol{\nu}(\mathbf{v}_R^*) - \boldsymbol{\nu}(\mathbf{v}_R^r) - \sum_{k=1}^{m-1} \mathbf{z}_k^* \right), \quad (\text{B.4})$$

and proving that those equations are equivalent to (13a) and (13b). Clearly (B.3) is equivalent to (13a). To get (13b), one can sum (B.3) from  $k=1$  to  $k=m-1$  and add the result to (B.4). This concludes the proof.

## Appendix C. Proof of Lemma 3

### Appendix C.1. Diffeomorphism

When trying to inverse  $T$ , the following is found:

$$\mathbf{z}_k = \psi_k + \mathbf{z}_k^* - \boldsymbol{\zeta}, \quad (k \in \llbracket 1, m-1 \rrbracket), \quad (\text{C.1a})$$

$$\boldsymbol{\zeta} = \boldsymbol{\zeta} + \boldsymbol{\zeta}^*, \quad (\text{C.1b})$$

$$\frac{1}{2} \varepsilon k_{iP} C_R \mathbf{v}_R^2 = \boldsymbol{\nu}(\mathbf{v}_R^r) - m\boldsymbol{\zeta} + \sum_{k=1}^m \psi_k, \quad (\text{C.1c})$$

$$\mathbf{i}_k = i_k + \mathbf{i}_k^*, \quad (k \in \llbracket 1, m \rrbracket), \quad (\text{C.1d})$$

$$\mathbf{v}_k = v_k + \mathbf{v}_k^*, \quad (k \in \llbracket 1, m \rrbracket), \quad (\text{C.1e})$$

$$\mathbf{i}_{Gk} = i_{Gk} + \mathbf{i}_{Gk}^*, \quad (k \in \llbracket 1, m \rrbracket), \quad (\text{C.1f})$$

where the definition of  $\boldsymbol{\nu}$  has been used. Clearly, there is no  $\mathbf{v}_R$  solving (C.1c) if the right hand-side of this equation is not strictly positive, since  $\varepsilon k_{iP} C_R > 0$ . Conversely, if this condition is satisfied, then there exists a unique  $\mathbf{v}_R > 0$  satisfying (C.1c). This proves that (C.1) with

$$\mathbf{v}_R = \sqrt{\frac{2}{\varepsilon k_{iP} C_R} \left( \boldsymbol{\nu}(\mathbf{v}_R^r) - m\boldsymbol{\zeta} + \sum_{k=1}^m \psi_k \right)}, \quad (\text{C.2})$$

in place of (C.1c) defines the inverse of the restriction of  $T$  on  $\mathcal{X}$  and that  $T(\mathcal{X})$  reads

$$\left\{ (\psi_1, \dots, \psi_m, \boldsymbol{\zeta}, \eta_1, \dots, \eta_m) : \boldsymbol{\nu}(\mathbf{v}_R^r) - m\boldsymbol{\zeta} + \sum_{k=1}^m \psi_k > 0 \right\}.$$

To conclude, it remains to mention that both  $T$  and  $T^{-1}$  are  $\mathcal{C}^1$  on  $\mathcal{X}$  and  $T(\mathcal{X})$ , respectively.

### Appendix C.2. Dynamics in the new coordinates

The  $m - 1$  first duty cycles write

$$\mathbf{d}_k = \frac{1}{\mathbf{v}_R} (k_p \mathbf{i}_k + \mathbf{z}_k + \zeta), \quad (\text{C.3})$$

$$\stackrel{(14a)}{=} \frac{1}{\mathbf{v}_R} (k_p \mathbf{i}_k + \psi_k + \mathbf{z}_k^* + \zeta^*), \quad (\text{C.4})$$

$$\stackrel{(13a)}{=} \frac{1}{\mathbf{v}_R} (k_p \mathbf{i}_k + \psi_k + \mathbf{v}_k^* - k_p \mathbf{i}_k^*). \quad (\text{C.5})$$

The last duty cycle writes

$$\mathbf{d}_m = \frac{1}{\mathbf{v}_R} \left( k_p \mathbf{i}_m + \zeta + \boldsymbol{\nu}(\mathbf{v}_R) - \boldsymbol{\nu}(\mathbf{v}_R^r) - \sum_{k=1}^{m-1} \mathbf{z}_k \right), \quad (\text{C.6})$$

$$\stackrel{(14b)}{=} \frac{1}{\mathbf{v}_R} \left( k_p \mathbf{i}_m + \psi_m + \zeta^* - \sum_{k=1}^{m-1} \mathbf{z}_k^* \right), \quad (\text{C.7})$$

where by (13a),  $\zeta^* - \sum_{k=1}^{m-1} \mathbf{z}_k^*$  equals

$$\zeta^* - \sum_{k=1}^{m-1} (\mathbf{v}_k^* - k_p \mathbf{i}_k^* - \zeta^*), \quad (\text{C.8})$$

$$= m\zeta^* - \sum_{k=1}^{m-1} (\mathbf{v}_k^* - k_p \mathbf{i}_k^*), \quad (\text{C.9})$$

$$\stackrel{(13b)}{=} \sum_{k=1}^m (\mathbf{v}_k^* - k_p \mathbf{i}_k^*) - \sum_{k=1}^{m-1} (\mathbf{v}_k^* - k_p \mathbf{i}_k^*), \quad (\text{C.10})$$

$$= \mathbf{v}_m^* - k_p \mathbf{i}_m^*. \quad (\text{C.11})$$

It follows that for all  $k \in \llbracket 1, m \rrbracket$ ,

$$\mathbf{d}_k = \frac{1}{\mathbf{v}_R} (k_p \mathbf{i}_k + \psi_k + \mathbf{v}_k^* - k_p \mathbf{i}_k^*), \quad (\text{C.12})$$

$$\stackrel{(C.1d)}{=} \frac{1}{\mathbf{v}_R} (k_p i_k + \psi_k + \mathbf{v}_k^*). \quad (\text{C.13})$$

Compute now the dynamics of  $\psi_k$ , ( $k \in \llbracket 1, m - 1 \rrbracket$ ):

$$\dot{\psi}_k \stackrel{(14a)}{=} \dot{\zeta} + \dot{\mathbf{z}}_k, \quad (\text{C.14})$$

$$\stackrel{(11a)}{=} \dot{\zeta} + \varepsilon k_{iP} (\mathbf{i}_k \mathbf{v}_R \mathbf{d}_k - \mathbf{P}_k^r), \quad (\text{C.15})$$

and, for  $k = m$ , using the definition of  $\psi_m$  in (14b), of  $\boldsymbol{\nu}$  in (12) and the dynamics of  $\mathbf{v}_R$  in (2a),

$$\dot{\psi}_m = \dot{\zeta} + \varepsilon k_{iP} \sum_{k=1}^m (\mathbf{i}_k \mathbf{v}_R \mathbf{d}_k) - \sum_{k=1}^{m-1} \dot{\mathbf{z}}_k, \quad (\text{C.16})$$

$$\stackrel{(11a)}{=} \dot{\zeta} + \varepsilon k_{iP} \sum_{k=1}^m (\mathbf{i}_k \mathbf{v}_R \mathbf{d}_k) - \varepsilon k_{iP} \sum_{k=1}^{m-1} (\mathbf{i}_k \mathbf{v}_R \mathbf{d}_k - \mathbf{P}_k^r), \quad (\text{C.17})$$

$$\stackrel{(7)}{=} \dot{\zeta} + \varepsilon k_{iP} (\mathbf{i}_m \mathbf{v}_R \mathbf{d}_m - \mathbf{P}_m^r). \quad (\text{C.18})$$

It follows that for all  $k \in \llbracket 1, m \rrbracket$ ,

$$\dot{\psi}_k = \dot{\zeta} + \varepsilon k_{iP} (\mathbf{i}_k \mathbf{v}_R \mathbf{d}_k - \mathbf{P}_k^r), \quad (\text{C.19})$$

$$\stackrel{(C.13), (C.1d)}{=} \dot{\zeta} + \varepsilon k_{iP} ((i_k + \mathbf{i}_k^*) (k_p i_k + \psi_k + \mathbf{v}_k^*) - \mathbf{P}_k^r), \quad (\text{C.20})$$

$$\stackrel{\text{Lem. 2}}{=} \dot{\zeta} + \varepsilon k_{iP} ((i_k + \mathbf{i}_k^*) (k_p i_k + \psi_k) + i_k \mathbf{v}_k^*), \quad (\text{C.21})$$

where (A.1e) has been used. Indeed, Lem. 2 states that  $\mathbf{P}_k^* = \mathbf{P}_k^r$ , ( $k \in \llbracket 1, m - 1 \rrbracket$ ). However, this is also true for  $k = m$ , as shown in (A.6). Eventually,

$$\dot{\zeta} = \dot{\zeta} \stackrel{(11b)}{=} \varepsilon k_{iv} (\boldsymbol{\nu}(\mathbf{v}_R) - \boldsymbol{\nu}(\mathbf{v}_R^r)), \quad (\text{C.22})$$

$$\stackrel{(C.1c)}{=} \varepsilon k_{iv} \left( -m\zeta + \sum_{k=1}^m \psi_k \right), \quad (\text{C.23})$$

which can be used in (C.21) to find (15a).

The remainder of the proof is focused on (2b), (2c) and (2d) from the PFC model. In (2b), replace  $\mathbf{d}_k$  by (C.13). Also use (C.1d), (C.1e) and (C.1f).

$$\begin{aligned} \frac{d}{dt} i_k &= \frac{d}{dt} \mathbf{i}_k = \frac{1}{L} (v_k + \mathbf{v}_k^* - (k_p i_k + \psi_k + \mathbf{v}_k^*)), \\ \frac{d}{dt} v_k &= \frac{d}{dt} \mathbf{v}_k = \frac{1}{C} (i_{Gk} + \mathbf{i}_{Gk}^* - (i_k + \mathbf{i}_k^*)), \\ \frac{d}{dt} i_{Gk} &= \frac{d}{dt} \mathbf{i}_{Gk} = \frac{1}{L_{Gk}} (V_{Gk} - (v_k + \mathbf{v}_k^*) - R_{Gk} (i_{Gk} + \mathbf{i}_{Gk}^*)). \end{aligned}$$

Using (13d),

$$\begin{cases} \frac{d}{dt} i_k &= \frac{1}{L} (v_k - k_p i_k - \psi_k), \\ \frac{d}{dt} v_k &= \frac{1}{C} (i_{Gk} - i_k), \\ \frac{d}{dt} i_{Gk} &= \frac{1}{L_{Gk}} (-v_k - R_{Gk} i_{Gk}), \end{cases} \quad (\text{C.24})$$

$$\iff \dot{\eta}_k = A_k(\theta) \eta_k + B \psi_k, \quad (\text{C.25})$$

where  $A_k(\theta)$  and  $B$  are defined in the statement of the Lemma. This concludes the proof.

### Appendix D. Proof of Proposition 1

Consider the following system

$$\dot{\omega} = A_k(\theta) \omega. \quad (\text{D.1})$$

Take the positive definite Lyapunov function  $H_k(\omega) = \frac{1}{2} \omega^\top P_k(\theta) \omega$ , with  $P_k(\theta) = \text{diag}\{[L \ C \ L_{Gk}]\}$ . Its derivative along the trajectories of (D.1) are

$$\dot{H}_k(\omega) = \frac{1}{2} \omega^\top (P_k(\theta) A_k(\theta) + A_k(\theta)^\top P_k(\theta)) \omega, \quad (\text{D.2})$$

$$= \omega^\top \text{diag}\{[-k_p, 0, -R_{Gk}]\} \omega \leq 0, \quad \forall \theta \in \Theta. \quad (\text{D.3})$$

Using LaSalle's theorem, the origin is shown to be exponentially stable. Note the following kernel:  $\mathcal{K}_H := \{\omega : \dot{H}_k(\omega) = 0\} = \text{Im}\{[0 \ 1 \ 0]^\top\}$ . For all element  $\omega = [\omega_1, \omega_2, \omega_3]^\top$  of this kernel,  $\omega_1 \equiv \omega_3 \equiv 0$ , and therefore,

$$0 \equiv \frac{d}{dt} \omega_3 = -\frac{1}{L_{Gk}} \omega_2. \quad (\text{D.4})$$

It follows that  $\omega_2 \equiv 0$ , and  $\omega \equiv \mathbf{0}$ . Note that if  $k_p = 0$ , the same conclusion is found, as  $\omega_3 \equiv 0 \Rightarrow \omega_2 \equiv 0 \Rightarrow \omega_1 \equiv 0$ . Hence the origin of (D.1) is globally asymptotically stable, for all  $\theta \in \Theta$ , hence for all  $(\theta, r) \in \mathcal{S}$ . It follows that  $A_k(\theta)$  is Hurwitz for all  $k$  and all  $(\theta, r) \in \mathcal{S}$ .

The two consequences are

- $A_k(\theta)$  is invertible, hence the equilibrium of (20) is unique and given by  $\mathbf{0} = g(x, h(x)) \iff h_k(x) = -A_k(\theta)^{-1} B \psi_k$ , ( $k \in \llbracket 1, m \rrbracket$ ), which yields (21).

- The system (20) is composed of  $m$  independent affine subsystems whose dynamic matrices are Hurwitz, its unique equilibrium point is therefore globally exponentially stable.
- No condition on  $x$  is required, hence the properties hold uniformly in  $x$ .

This concludes the proof.

## Appendix E. Proof of Proposition 2

With  $\eta_k = h_k(x)$  given by (21), the calculus given in Appendix E.1 leads to:

$$f(x, h(x)) = \begin{bmatrix} k_{iP}(-a_1\psi_1^2 - b_1\psi_1) + k_{iv}(-m\zeta + \sum_{k=1}^m \psi_k) \\ \vdots \\ k_{iP}(-a_m\psi_m^2 - b_m\psi_m) + k_{iv}(-m\zeta + \sum_{k=1}^m \psi_k) \\ k_{iv}(-m\zeta + \sum_{k=1}^m \psi_k) \end{bmatrix}, \quad (\text{E.1})$$

where

$$a_k = \frac{R_{Gk}}{(R_{Gk} + k_p)^2} \quad \text{and} \quad b_k = \frac{1}{R_{Gk} + k_p} (2V_k^* - V_{Gk}). \quad (\text{E.2})$$

*Analysis of the stability.* Take the following Lyapunov candidate

$$V(x) = \frac{1}{2}m\zeta^2 + \frac{1}{2} \sum_{k=1}^m \psi_k^2. \quad (\text{E.3})$$

Evaluating  $V$  along the trajectories of  $f$ , where  $f_k$  is the  $k$ -th line of  $f$ , leads to

$$\begin{aligned} \frac{\partial V}{\partial x} f(x, h(x)) &= m\zeta f_{m+1}(x, h(x)) + \sum_{k=1}^m \psi_k f_k(x, h(x)), \\ &= -m^2 k_{iv} \zeta^2 + m k_{iv} \zeta \sum_{k=1}^m \psi_k \\ &\quad + \sum_{k=1}^m \psi_k \left( k_{iP}(-a_k \psi_k^2 - b_k \psi_k) + k_{iv}(-m\zeta + \sum_{i=1}^m \psi_i) \right), \\ &= -m^2 k_{iv} \zeta^2 + m k_{iv} \zeta \sum_{k=1}^m \psi_k - \sum_{k=1}^m \psi_k k_{iv} m \zeta \\ &\quad + \sum_{k=1}^m (k_{iP}(-a_k \psi_k - b_k) \psi_k^2) + k_{iv} \sum_{k=1}^m \sum_{i=1}^m \psi_k \psi_i. \end{aligned}$$

The following Lemma, proven in Appendix E.2 allows to find a bound on the derivative of the Lyapunov function.

**Lemma 4.** For any  $\psi_{k,i} \in \mathbb{R}$ , ( $k, i \in \llbracket 1, m \rrbracket$ )

$$\sum_{k=1}^m \sum_{i=1}^m \psi_k \psi_i \leq m \sum_{k=1}^m \psi_k^2. \quad (\text{E.4})$$

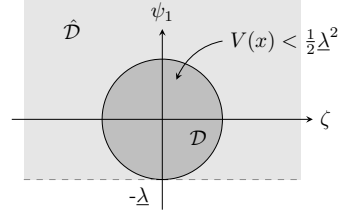


Figure E.11: illustration of the estimation of the basin of attraction of the slow subsystem for  $m = 1$ .

The bound then writes

$$\begin{aligned} \frac{\partial V}{\partial x} f(x, h(x)) &\leq -m^2 k_{iv} \zeta^2 - \sum_{k=1}^m k_{iP} (a_k \psi_k + b_k) \psi_k^2 + m k_{iv} \sum_{k=1}^m \psi_k^2, \\ &\leq -m^2 k_{iv} \zeta^2 - \sum_{k=1}^m (k_{iP} (a_k \psi_k + b_k) - m k_{iv}) \psi_k^2. \end{aligned} \quad (\text{E.5})$$

$$\leq -m^2 k_{iv} \zeta^2 - \sum_{k=1}^m (k_{iP} (a_k \psi_k + b_k) - m k_{iv}) \psi_k^2. \quad (\text{E.6})$$

The next lemma allows to find the final bound on the Lyapunov. Its proof can be found in Appendix E.3.

**Lemma 5.** Given  $k_{iv}$  and  $k_{iP}$  selected as in Th. 1 and  $\lambda$  selected as in Prop. 2, there exists  $\kappa > 0$  such that the following holds :

$$m^2 k_{iv} > \frac{1}{2} \kappa m \quad (\text{E.7})$$

and

$$k_{iP} (a_k \psi_k + b_k) - m k_{iv} > \frac{1}{2} \kappa, \quad (k \in \llbracket 1, m \rrbracket), \quad (\text{E.8})$$

for all  $(\theta, r) \in \mathcal{S}$  and all  $\psi_k > -\lambda$ .

Therefore, there exists  $\kappa > 0$  such that

$$\frac{\partial V}{\partial x} f(x, h(x)) < -\kappa \left( \frac{1}{2} m \zeta^2 + \frac{1}{2} \sum_{k=1}^m \psi_k^2 \right) \stackrel{(\text{E.3})}{=} -\kappa V(x) \quad (\text{E.9})$$

for all  $\psi_k > -\lambda$  and all  $k$ . Since  $V$  is a positive definite quadratic Lyapunov function, it can be concluded from (E.9) that the origin of (23) is locally exponentially stable for all  $(\theta, r) \in \mathcal{S}$ .

*Estimation of the basin of attraction.* It has been shown that  $\dot{V}(x) < -\kappa V(x) \forall x \in \hat{\mathcal{D}} := \{x \in \mathbb{R}^{m+1} : \psi_k > -\lambda, (k \in \llbracket 1, m \rrbracket)\}$ . It is possible to find an inner estimate of the basin of attraction by including a level set of the chosen Lyapunov function in  $\hat{\mathcal{D}}$ :

$$\mathcal{D} = \left\{ x \in \mathbb{R}^{m+1} : V(x) = \frac{1}{2} m \zeta^2 + \frac{1}{2} \sum_{k=1}^m \psi_k^2 < c \right\}$$

where  $c$  is chosen such that  $\mathcal{D} \subset \hat{\mathcal{D}}$ , that is,  $c = \frac{1}{2} \lambda^2$ . An illustrative example for  $m = 1$  is shown in Fig. E.11.

*Appendix E.1. Detail of the calculus leading to (E.1)*

Pick any  $k \in \llbracket 1, m \rrbracket$ . Beforehand, note that using (21),

$$k_p i_k + \psi_k = \frac{-\psi_k}{R_{Gk} + k_p} k_p + \psi_k, \quad (\text{E.10})$$

$$= \frac{-k_p + R_{Gk} + k_p}{R_{Gk} + k_p} \psi_k. \quad (\text{E.11})$$

Hence,

$$(i_k + \mathbf{i}_k^*)(k_p i_k + \psi_k) + i_k \mathbf{v}_k^* = -a_k \psi_k^2 - b_k \psi_k, \quad (\text{E.12})$$

where (13d) and (E.2) have been used.

*Appendix E.2. Proof of Lemma 4*

For any scalars  $\psi_{k,i} \in \mathbb{R}$ , ( $k, i \in \llbracket 1, m \rrbracket$ )

$$\begin{aligned} \sum_{k=1}^m \sum_{i=1}^m \psi_k \psi_i &= \sum_{k=1}^m \left( \psi_k \psi_k + \sum_{\substack{i=1 \\ i \neq k}}^m \psi_k \psi_i \right), \\ &= \sum_{k=1}^m (\psi_k^2) + \sum_{k=1}^m \sum_{\substack{i=1 \\ i \neq k}}^m (\psi_k \psi_i). \end{aligned}$$

Moreover, for any  $\psi_{k,i} \in \mathbb{R}$ ,

$$(\psi_k - \psi_i)^2 = \psi_k^2 + \psi_i^2 - 2\psi_k \psi_i \geq 0, \quad (\text{E.13})$$

$$\iff \psi_k \psi_i \leq \frac{1}{2}(\psi_k^2 + \psi_i^2). \quad (\text{E.14})$$

it follows that

$$\begin{aligned} \sum_{k=1}^m \sum_{i=1}^m \psi_k \psi_i &\leq \sum_{k=1}^m (\psi_k^2) + \frac{1}{2} \sum_{k=1}^m \sum_{\substack{i=1 \\ i \neq k}}^m (\psi_k^2 + \psi_i^2), \\ &\leq \sum_{k=1}^m (\psi_k^2) + \frac{1}{2} \sum_{k=1}^m \sum_{\substack{i=1 \\ i \neq k}}^m (\psi_k^2) + \frac{1}{2} \sum_{k=1}^m \sum_{\substack{i=1 \\ i \neq k}}^m (\psi_i^2), \\ &\leq \sum_{k=1}^m (\psi_k^2) + \frac{1}{2}(m-1) \sum_{k=1}^m (\psi_k^2) + \frac{1}{2}(m-1) \sum_{k=1}^m (\psi_k^2), \\ &\leq m \sum_{k=1}^m (\psi_k^2), \end{aligned}$$

which concludes the proof

*Appendix E.3. Proof of Lemma 5*

Pick any  $k \in \llbracket 1, m \rrbracket$ . Recall that both  $a_k$  and  $b_k$ , given in (E.2) depend on  $(\theta, r)$ . Select

$$\lambda_k := \frac{b_k - \delta / (R_{Gk} + k_p)}{a_k}. \quad (\text{E.15})$$

$$\lambda_k \stackrel{(\text{E.2})}{=} \frac{R_{Gk} + k_p}{R_{Gk}} (2\mathbf{v}_k^* - V_{Gk} - \delta).$$

Since i)  $R_{Gk} \mapsto \frac{R_{Gk} + k_p}{R_{Gk}}$  is strictly positive and decreasing on  $\mathbb{R}_{>0}$  and  $R_{Gk} \in [\underline{R}, \bar{R}]$ , ii)  $\mathbf{v}_k^* \in ]\underline{\mathbf{v}}, \bar{\mathbf{v}}[$  by Lem. 2, iii)

$V_{Gk} \in [0, \bar{\mathbf{v}}]$  by definition of  $\Theta$  and iv)  $\delta < \mathbf{v}^n - 3\Delta \mathbf{v} = 2\mathbf{v} - \bar{\mathbf{v}}$  by statement of Thm. 1, it follows that for all  $(\theta, r) \in \mathcal{S}$ ,

$$\lambda_k \geq \frac{\bar{R} + k_p}{\bar{R}} (2\mathbf{v} - \bar{\mathbf{v}} - \delta) \stackrel{(24)}{=} \underline{\lambda} > 0. \quad (\text{E.16})$$

Then, for all  $\psi_k > -\underline{\lambda}$  and all  $(\theta, r) \in \mathcal{S}$

$$\begin{aligned} a_k \psi_k + b_k &\geq b_k - a_k \underline{\lambda} \stackrel{(\text{E.16})}{\geq} b_k - a_k \lambda_k \\ &\stackrel{(\text{E.15})}{=} \frac{\delta}{R_{Gk} + k_p} \geq \frac{\delta}{\bar{R} + k_p} \stackrel{(10)}{=} l(\delta) > 0. \end{aligned} \quad (\text{E.17})$$

Moreover, according to the statement of Prop. 2,  $k_{iv} > 0$  and  $k_{iP} > mk_{iv}/l(\delta)$ . Then, there exists an  $\kappa > 0$  sufficiently small such that

$$k_{iv} > \frac{\kappa}{2m} \quad \text{and} \quad k_{iP} - \frac{mk_{iv}}{l(\delta)} > \frac{\frac{1}{2}\kappa}{l(\delta)}, \quad (\text{E.18})$$

It follows that

$$m^2 k_{iv} > \frac{1}{2} \kappa m \quad (\text{E.19})$$

and

$$k_{iP} l(\delta) - mk_{iv} > \frac{1}{2} \kappa. \quad (\text{E.20})$$

Using (E.17), it follows that for all  $(\theta, r) \in \mathcal{S}$  and  $\psi_k > -\underline{\lambda}$ ,

$$k_{iP}(a_k \psi_k + b_k) - mk_{iv} > \frac{1}{2} \kappa, \quad (\text{E.21})$$

which concludes the proof.

## References

- Anand, S., Fernandes, B.G., 2010. Optimal voltage level for DC microgrids, in: IECON 2010 - 36th Annual Conference on IEEE Industrial Electronics Society, IEEE, Glendale, AZ, USA. pp. 3034–3039. doi:10.1109/IECON.2010.5674947.
- Astolfi, D., Praly, L., 2017. Integral Action in Output Feedback for Multi-Input Multi-Output Nonlinear Systems. IEEE Transactions on Automatic Control 62, 1559–1574. doi:10.1109/TAC.2016.2599784.
- Balasubramaniam, S., Ugalde-Loo, C.E., Liang, J., 2019. Series Current Flow Controllers for DC Grids. IEEE Access 7, 14779–14790. doi:10.1109/ACCESS.2019.2893450.
- Barara, M., Morel, H., Clerc, G., 2017. Control Strategy Scheme for Consistent Power Flow Control in Meshed DC Micro-grids, in: International Conference on Components and Systems for DC Grids, Grenoble, France.
- Benedito, E., del Puerto-Flores, D., Dòria-Cerezo, A., Scherpen, J.M.A., 2019. Port-Hamiltonian based Optimal Power Flow algorithm for multi-terminal DC networks. Control Engineering Practice 83, 141–150. doi:10.1016/j.conengprac.2018.10.018.
- Caramizaru, A., Uihlein, A., 2020. Energy communities: an overview of energy and social innovation. Technical Report EUR 30083 EN. European Commission, Joint Research Center. URL: <https://data.europa.eu/doi/10.2760/180576>.
- Casavola, A., Tedesco, F., Vizza, M., 2017. A Command Governor Approach for the Voltage Control in Smart Grids with Distributed Generation and Storage Devices. IFAC-PapersOnLine 50, 10003–10008. doi:10.1016/j.ifacol.2017.08.2033.
- Cisneros, R., Pirro, M., Bergna, G., Ortega, R., Ippoliti, G., Molinas, M., 2015. Global tracking passivity-based PI control of bilinear systems: Application to the interleaved boost and modular multilevel converters. Control Engineering Practice, 109–119. doi:10.1016/j.conengprac.2015.07.002.

- Cucuzzella, M., Trip, S., De Persis, C., Cheng, X., Ferrara, A., van der Schaft, A., 2019. A Robust Consensus Algorithm for Current Sharing and Voltage Regulation in DC Microgrids. *IEEE Transactions on Control Systems Technology* 27, 1583–1595. doi:10.1109/TCST.2018.2834878.
- Fotopoulou, M., Rakopoulos, D., Trigkas, D., Stergiopoulos, F., Blanas, O., Voutetakis, S., 2021. State of the Art of Low and Medium Voltage Direct Current (DC) Microgrids. *Energies* 14, 5595–5620. doi:10.3390/en14185595.
- Grasselli, O., Isidori, A., Nicolo, F., 1979. Output regulation of a class of bilinear systems under constant disturbances. *Automatica* 15, 189–195. doi:10.1016/0005-1098(79)90069-4.
- Gutman, P.O., 1981. Stabilizing controllers for bilinear systems. *IEEE Transactions on Automatic Control* 26, 917–922. doi:10.1109/TAC.1981.1102742.
- Hatzigargyriou, N., 2014. *Microgrids Architectures and control*. John Wiley & Sons.
- IEEE-SA, 2009. *IEEE Std 1159™-2009, IEEE Recommended Practice for Monitoring Electric Power Quality*. Technical Report IEEE Std 1159™ -2009. IEEE Power & Energy Society.
- Jeeninga, M., Persis, C.D., van der Schaft, A.J., 2020. Plug-and-play Solvability of the Power Flow Equations for Interconnected DC Microgrids with Constant Power Loads. *IFAC-PapersOnLine* 53, 13005–13011. doi:10.1016/j.ifacol.2020.12.2158.
- Jovic, D., Ooi, B.T., 2010. Developing DC Transmission Networks Using DC Transformers. *IEEE Transactions on Power Delivery* 25, 2535–2543. doi:10.1109/TPWRD.2010.2052074.
- K.Khalil, H., 2002. *Nonlinear Systems*. 3rd ed., Prentice Hall.
- Kockel, C., Nolting, L., Goldbeck, R., Wulf, C., De Doncker, R.W., Praktikno, A., 2022. A scalable life cycle assessment of alternating and direct current microgrids in office buildings. *Applied Energy* 305, 117878. doi:10.1016/j.apenergy.2021.117878.
- Lin-Shi, X., Simon, T., Tréguët, J.F., Morel, H., 2021. Flatness-Based Control of an m-Branch Power Flow Controller for Meshed DC Microgrids, in: 2021 IEEE 1st International Power Electronics and Application Symposium (PEAS). doi:10.1109/PEAS53589.2021.9628872.
- Longchamp, R., 1980. Stable feedback control of bilinear systems. *IEEE Transactions on Automatic Control* 25, 302–306. doi:10.1109/TAC.1980.1102303.
- Mackay, L., Blij, N.H.v.d., Ramirez-Elizondo, L., Bauer, P., 2017. Toward the Universal DC Distribution System. *Electric Power Components and Systems* 45, 1532–5016. doi:10.1080/15325008.2017.1318977.
- Mackay, L., Hailu, T., Ramirez-Elizondo, L., Bauer, P., 2015. Decentralized current limiting in meshed DC distribution grids, in: 2015 IEEE First International Conference on DC Microgrids (ICDCM), pp. 234–238. doi:10.1109/ICDCM.2015.7152045.
- Nasirian, V., Moayedi, S., Davoudi, A., Lewis, F.L., 2015. Distributed Cooperative Control of DC Microgrids. *IEEE Transactions on Power Electronics* 30, 2288–2303. doi:10.1109/TPEL.2014.2324579.
- Natori, K., Nakao, Y., Sato, Y., 2018. A Novel Control Approach to Multi-Terminal Power Flow Controller for Next-Generation DC Power Network, in: 2018 International Power Electronics Conference (IPEC-Niigata 2018 -ECCE Asia), pp. 588–592. doi:10.23919/IPEC.2018.8507609.
- Natori, K., Tanaka, T., Takahashi, Y., Sato, Y., 2017. A study on high-efficiency floating multi-terminal power flow controller for next-generation DC power networks, in: 2017 IEEE Energy Conversion Congress and Exposition (ECCE), IEEE, Cincinnati, OH. pp. 2631–2637. doi:10.1109/ECCE.2017.8096497.
- Prakash, K., Lallu, A., Islam, F., Mamun, K., 2016. Review of Power System Distribution Network Architecture, in: 2016 3rd Asia-Pacific World Congress on Computer Science and Engineering (APWC on CSE), Nadi, Fiji. pp. 124–130. doi:10.1109/APWC-on-CSE.2016.030.
- Purgat, P., Mackay, L., Adilardi Prakoso, R., Ramirez-Elizondo, L., Bauer, P., 2017. Power flow control converter for meshed LVDC distribution grids, in: 2017 IEEE Second International Conference on DC Microgrids (ICDCM), IEEE, Nuremburg, Germany. pp. 476–483. doi:10.1109/ICDCM.2017.8001089.
- Ramirez, V., Ortega, R., Bethoux, O., Sánchez-Squella, A., 2014. A dynamic router for microgrid applications: Theory and experimental results. *Control Engineering Practice* 27, 23–31. doi:10.1016/j.conengprac.2014.02.005.
- Saberi, A., Khalil, H., 1984. Quadratic-type Lyapunov functions for singularly perturbed systems. *IEEE Transactions on Automatic Control* doi:10.1109/TAC.1984.1103586.
- Simon, T., Giaccagli, M., Tréguët, J.F., Astolfi, D., Andrieu, V., Lin-Shi, X., Morel, H., 2021a. Robust Output Set-Point Tracking for a Power Flow Controller via Forwarding Design, in: 2021 60th IEEE Conference on Decision and Control (CDC).
- Simon, T., Tréguët, J.F., Morel, H., Lin-Shi, X., 2021b. Modelling and Control of a Power Flow Controller for DC Microgrids, in: 2021 23rd European Conference on Power Electronics and Applications (EPE'21 ECCE Europe).
- Takahashi, Y., Natori, K., Sato, Y., 2015. A multi-terminal power flow control method for next-generation DC power network, in: 2015 IEEE Energy Conversion Congress and Exposition (ECCE), IEEE, Montreal, QC, Canada. pp. 6223–6230. doi:10.1109/ECCE.2015.7310533.
- Tang, G.Y., Zhao, Y.D., Ma, H., 2006. Optimal output tracking control for bilinear systems. *Transactions of the Institute of Measurement and Control* 28, 387–397. doi:10.1177/0142331206073065.
- Tarbouriech, S., Queinnec, I., Calliero, T.R., Peres, P.L.D., 2009. Control design for bilinear systems with a guaranteed region of stability: An LMI-based approach, in: 2009 17th Mediterranean Conference on Control and Automation, IEEE, Thessaloniki, Greece. pp. 809–814. doi:10.1109/MED.2009.5164643.
- Vuyuru, U., Maiti, S., Chakraborty, C., 2019. Active Power Flow Control Between DC Microgrids. *IEEE Transactions on Smart Grid* 10, 5712–5723. doi:10.1109/TSG.2018.2890548.
- Zafeiratou, I., Prodan, I., Lefèvre, L., Piétrac, L., 2018. Dynamical modelling of a DC microgrid using a port-Hamiltonian formalism. *IFAC-PapersOnLine* 51, 469–474. doi:10.1016/j.ifacol.2018.03.079.
- Zitte, B., Hamroun, B., Astolfi, D., Couenne, F., 2020. Robust Control of a Class of Bilinear Systems by Forwarding: Application to Counter Current Heat Exchanger. *IFAC-PapersOnLine* 53, 11515–11520. doi:10.1016/j.ifacol.2020.12.603.